

NAS 1.14:D-8437

AUG 8 1977

NASA TECHNICAL NOTE

NASA TN D-8437



NASA TN D-8437

**COMPLETED
ORIGINAL**

**LOAD AND STABILITY MEASUREMENTS
ON A SOFT-INPLANE ROTOR SYSTEM
INCORPORATING ELASTOMERIC
LEAD-LAG DAMPERS**

William H. Weller

*Langley Directorate,
U.S. Army Air Mobility R&D Laboratory*

*Langley Research Center
Hampton, Va. 23665*

NATIONAL AERONAUTICS AND SPACE ADMINISTRATION • WASHINGTON, D. C. • JULY 1977

70

1. Report No. NASA TN D-8437	2. Government Accession No.	3. Recipient's Catalog No.	
4. Title and Subtitle LOAD AND STABILITY MEASUREMENTS ON A SOFT-INPLANE ROTOR SYSTEM INCORPORATING ELASTOMERIC LEAD-LAG DAMPERS		5. Report Date July 1977	
7. Author(s) William H. Weller		6. Performing Organization Code	
9. Performing Organization Name and Address Langley Directorate, USAAMRDL NASA Langley Research Center Hampton, VA 23665		8. Performing Organization Report No. L-11315	
12. Sponsoring Agency Name and Address National Aeronautics and Space Administration Washington, DC 20546 an.l U.S. Army Air Mobility R&D Laboratory Moffett Field, CA 94035		10. Work Unit No. 505-10-26-01	
15. Supplementary Notes		11. Contract or Grant No.	
		13. Type of Report and Period Covered Technical Note	
		14. Army Project No. 1L262209AH76	
16. Abstract An experimental investigation has been conducted of the dynamic response and inplane stability associated with a new soft-inplane helicopter rotor. The unique feature of this rotor was the use of an internal elastomeric damper to restrain the blade inplane motion about the lead-lag hinge. The properties of the elastomer were selected to provide both a nominal first inplane frequency ratio of 0.65 and sufficient damping to eliminate the need for additional external damping sources to prevent ground resonance on a typical fuselage structure. For this investigation a 1/5-scale aeroelastic model was used to represent the rotor. The four-blade model had a diameter of 3.05 m (10 ft) and a solidity of 0.103. The first out-of-plane frequency ratio was 1.06.			
 The model was tested in hover and in forward flight up to an advance ratio of 0.45. At each forward speed the rotor lift was varied up to simulated maneuver conditions. The measured rotor loads and response were within acceptable limits, and no adverse response qualities were observed. Moderate out-of-plane hub moments were measured, even for zero lift, to indicate the beneficial control power available for this design. Blade inplane stability testing indicated that the rotor system damping remained at moderate levels throughout the operating envelope. The damping provided by the elastomer was supplemented by damping arising from favorable kinematic and blade aeroelastic coupling. Results of this investigation are applicable to rotor aeroelastic and dynamic stability characteristics of rotor systems.			
17. Key Words (Suggested by Author(s)) Soft-inplane rotor Rotor dynamic response Blade inplane stability Rotor performance Generalized rotor aeroelastic model Model rotor testing		18. Distribution Statement Unclassified - Unlimited	
Subject Category 05			
19. Security Classif. (of this report) Unclassified	20. Security Classif. (of this page) Unclassified	21. No. of Pages 68	22. Price* \$4.50

* For sale by the National Technical Information Service, Springfield, Virginia 22161

LOAD AND STABILITY MEASUREMENTS ON A SOFT-INPLANE ROTOR SYSTEM
INCORPORATING ELASTOMERIC LEAD-LAG DAMPERS

William H. Weller*

Langley Research Center

SUMMARY

An experimental investigation has been conducted of the dynamic response and inplane stability associated with a new soft-inplane helicopter rotor. The unique feature of this rotor was the use of an internal elastomeric damper to restrain the blade inplane motion about the lead-lag hinge. The properties of the elastomer were selected to provide both a nominal first inplane frequency ratio of 0.65 and sufficient damping to eliminate the need for additional external damping sources to prevent ground resonance on a typical fuselage structure. For this investigation a 1/5-scale aeroelastic model was used to represent the rotor. The four-blade model had a diameter of 3.05 m (10 ft) and a solidity of 0.103. The first out-of-plane frequency ratio was 1.06.

The model was tested in hover and in forward flight up to an advance ratio of 0.45. At each forward speed the rotor lift was varied up to simulated maneuver conditions. The measured rotor loads and response were within acceptable limits, and no adverse response qualities were observed. Moderate out-of-plane hub moments were measured, even for zero lift, to indicate the beneficial control power available for this design. Blade inplane stability testing indicated that the rotor system was free of instabilities involving the blade inplane degree of freedom and that the rotor damping remained at moderate levels throughout the operating envelope. The damping provided by the elastomer was supplemented by damping arising from favorable kinematic and blade aeroelastic coupling. The rotor simulated a soft-inplane hingeless design while providing additional inplane damping over that generally encountered on hingeless rotors without external dampers.

INTRODUCTION

Interest in hingeless-rotor systems has led to further consideration of the merits of soft-inplane rotors (inplane frequency below the rotor rotational frequency) for applications on small to moderate sized helicopters. References 1 and 2 describe a number of

*Langley Directorate, U.S. Army Air Mobility R&D Laboratory.

research and development programs associated with hingeless-rotor concepts. Due to their lack of flapping hinges, these rotors offer increased control power because of the hub moments resulting from blade out-of-plane aeroelastic deflections. In comparison to other configurations, hingeless-rotor designs often require less hardware which leads to reductions in aerodynamic drag and maintenance problems. In general, however, hingeless rotors can, and do, have certain problems inherent in their design. In the case of soft-inplane rotors, several aeroelastic instabilities are possible. Ground and air resonance can be catastrophic and result from dynamic coupling between the blade inplane motions and those of the support structure below the hub. Flap-lag instability may be encountered at high rotor thrust, and it is dependent on the isolated rotor characteristics. However, recent analytical and experimental studies (refs. 3 to 6) have provided some insight into these stability problems and to methods for their prevention.

An experimental investigation has been conducted of the aeroelastic response and stability associated with a new soft-inplane four-blade main rotor. This rotor, referred to as a Flexhinge rotor, incorporated lead-lag hinges with internal elastomeric dampers. Damper characteristics were selected to yield the required blade-lag frequency as well as damping sufficient to prevent ground and air resonance. For this investigation, the rotor was simulated by a 1/5-scale aeroelastic model designed and built by Bell Helicopter Textron. Bell Helicopter personnel also participated in the model tests. The model rotor was mounted on the generalized rotor aeroelastic model (GRAM) which is a universal model-rotor test stand used to simulate helicopter structure and control systems.

During the experimental program, extensive stability tests were carried out for the hovering case. The rotor was excited by control inputs at prescribed amplitudes and frequencies. Blade loads data and pylon motions were recorded on magnetic tape and later processed to identify the regressive inplane mode-response amplitude, frequency, and damping. In forward flight considerable dynamic response and performance data were collected at numerous flight speeds and trim conditions. A limited number of air-resonance stability checks were also performed. Representative performance, loads, and aeroelastic stability data resulting from this program are presented graphically in this report.

SYMBOLS

Values are given in SI Units and, where useful, also in U.S. Customary Units. Measurements and calculations were made in U.S. Customary Units.

b number of blades

C hub equivalent viscous damping, N-s/in

C_D	rotor drag coefficient, $\frac{D}{\pi R^2 \rho (\Omega R)^2}$
C_L	rotor lift coefficient, $\frac{L}{\pi R^2 \rho (\Omega R)^2}$
C_l	hub rolling-moment coefficient, $\frac{l}{\pi R^3 \rho (\Omega R)^2}$
$C_{l\alpha}$	rolling-moment-coefficient derivative with respect to shaft angle, per radian
C_m	hub pitching-moment coefficient, $\frac{m}{\pi R^3 \rho (\Omega R)^2}$
$C_{m\alpha}$	pitching-moment-coefficient derivative with respect to shaft angle, per radian
C_Q	rotor torque coefficient, $\frac{Q}{\pi R^3 \rho (\Omega R)^2}$
C_T	rotor thrust coefficient, $\frac{T}{\pi R^2 \rho (\Omega R)^2}$
c	blade chord, m
D	rotor drag force, N
g	gravitational constant, 9.8 m/s^2
K	hub equivalent stiffness, N/m
K_ζ	pitch-lag coupling (positive with lead and pitch up), deg/deg
L	rotor lift force, N
l	hub rolling moment, N-m
M	hub equivalent mass, kg
m	hub pitching moment, N-m
Q	rotor torque, N-m
R	blade radius, m
r	radial blade station measured from center of rotation, m

T	rotor thrust, N
V	forward velocity, m/s
x	nondimensional blade station measured from rotor center line, r/R
α_s	rotor shaft angle of attack (positive with fuselage nose-up), deg
ΔB_1	longitudinal cyclic change from zero flapping about shaft, deg
δ_3	pitch-flap coupling angle (positive with flap up and pitch down), deg
ζ	blade lead-lag angle (positive with lag aft), deg
$\theta_{0.75R}$	blade collective pitch angle at 0.75R, deg
μ	advance ratio, V/ ΩR
ρ	density of air, kg/m ³
σ	rotor solidity, bc/ πR
Ω	rotor rotational speed, rad/s

EXPERIMENTAL APPARATUS AND PROCEDURES

Test Facility

The experimental program was conducted at the Langley transonic dynamics tunnel (TDT). The TDT is a continuous-flow tunnel which is capable of operation over a Mach number range from 0 to 1.20 at pressures ranging from near 1380 N/m² (0.2 psia) to atmospheric pressure. Either air or Freon-12 may be used as a test medium, depending upon the flow conditions to be simulated. The tunnel test section is 4.9 m (16 ft) square with cropped corners and a cross-sectional area of 23 m² (248 ft²). Model blockage effects are diminished by the three slots in both the ceiling and floor which give an open surface area of 2.1 percent in the test section and by two sidewall slots on each side representing an additional 2.3-percent open area.

During the testing considerable use was made of the data acquisition system of the transonic dynamics tunnel. Off-line data reduction was also performed by using the computer system. The data system includes a digital computer, as well as transducer

signal conditioners, amplifiers, and calibration signal sources sufficient to handle 60 channels of data. From the amplifiers, data are routed through a patch panel to a direct-record FM tape recorder, and, simultaneously, through a multiplexing system, onto a frequency multiplexed FM tape. The direct-record tape can accept up to 12 channels of data. The multiplexing system can record 60 channels of data by multiplexing 5 channels on each track. Data from the signal amplifiers are also fed to a 60-channel analog-to-digital system and then to the system computer for processing. Control of the computer is exercised by a graphic display unit and associated keyboard. Peripheral equipment includes alternate typewriter, teletype, card reader, card punch, and line printer.

Generalized Rotor Aeroelastic Model

A schematic diagram of the generalized rotor aeroelastic model (GRAM) is shown in figure 1 along with overall dimensional data. This model serves as a powered test stand for evaluating the aeroelastic behavior of new rotor designs as well as providing a means for carrying out generalized research related to helicopter dynamics. Figure 2 presents a detailed view of the model and illustrates the more important features. The frame of the GRAM is constructed of welded steel plate which is attached by four linear springs to an internal base plate such that the model has freedom of motion in pitch, roll, and vertical translation with respect to the base plate. Full-scale rigid body or suspension-system frequencies can thus be simulated by proper selection of these mount springs. Steel rods can also be mounted to lock out the hub motions effectively. The complete frame is enclosed by a fiberglass and aluminum shell.

The GRAM rotor shaft is driven by two variable-frequency, water-cooled, electric synchronous motors. Each motor is rated at 35 kilowatts at a rotational speed of 1256 rad/s. The motors are connected to the rotor shaft through a two-stage speed-reduction system. The combined reduction of both stages is either 17.47:1 or 7.75:1, depending upon the motor pulleys and drive sheave used, and results in maximum rotor operating speeds of 71.9 or 162.1 rad/s, respectively. These two speed ranges are utilized for testing Mach scaled rotor models in Freon-12 and air, respectively. The lower speed may also be used in testing Froude scaled rotor models in air. The drive system is designed for 60 kilowatts continuous power at typical operating rotor speeds of 62.8 or 141.4 rad/s. Rotor speed is controlled by varying the electric line frequency to the synchronous motors.

The generalized rotor aeroelastic model features several controls which are remotely controlled. The pitch attitude of the model can be remotely changed by electro-mechanical actuators over a range from 20° nose-down to 8° nose-up. A remotely actuated horizontal stabilizer is provided to contribute to model stability in pitch and to

oppose body steady-state nose-up pitching moments. The model has a complete main-rotor control system. The swashplate, pictured in figures 2 and 3, is mounted on the rotor shaft below the rotor adapter flange and is raised or lowered by three assemblies combining a hydraulic actuator and an electric servo to achieve collective pitch changes and independent cyclic swashplate motions for rotor trimming purposes. For tests involving high-frequency control inputs, the hydraulic actuators are used for generating transient or sinusoidal inputs about the trim state. This is especially useful in determining rotor frequency response and subcritical stability characteristics.

The GRAM is instrumented to read all model control settings including model angle of attack, horizontal-tail incidence with respect to the fuselage reference line, collective pitch, lateral and longitudinal cyclic pitch, and selected rotor loads. The model geometric pitch attitude is measured by an angle transducer. The horizontal-tail and rotor-control measurements are made by linear or angular potentiometers. All three components of body translational acceleration are measured by accelerometers mounted on a common bracket as near to the fuselage center of gravity as practical. Rotor shaft speed is determined by a magnetic pickup on the model. The rotating-blade data are transferred to the fixed system through a 60-ring, horizontal-disk, slip-ring assembly by using two brushes per ring. The forces and moments of the combined rotor and fuselage are measured by a six-component balance mounted below the base plate and covered by an aluminum shroud. The balance is post mounted and does not rotate with the fuselage.

Model Rotor System

The test model, shown in figure 4, was a 3.05-m (10-ft) diameter, four-blade soft-inplane rotor with a solidity of 0.103, a Lock number of 7.6, and an operating speed of 64.4 rad/s. The blades were constructed of fiberglass with an aluminum honeycomb core. The blades had an NACA 0012 airfoil section, a constant 12.34-cm (4.86-in.) chord, and a twist distribution as shown in figure 5. The hub, pictured in figure 6, had a pair of soft flapping flexures inboard of the pitch bearing for each blade. The flexures were composed of an aluminum sheet with laminated fiberglass covering both sides to yield the selected hub flapping stiffness and coning shape. The first out-of-plane frequency ratio was 1.06, and the net precone built into the flexures was 4° for each blade. The flexures continued across the shaft attachment connecting blade grip assemblies for opposite blades. The rotor consisted of two such flexure pairs stacked vertically and resulting in two tip-path planes one blade thickness apart. The inboard pitch bearing and lag hinge were located in a common housing at 10 percent radius, as shown in figure 6. The outboard pitch bearing and lead-lag damper housing were connected to the flapping flexures by the pitch spindle which was swept aft by 1.9° . Thus, the unloaded

blade and feathering axes were both swept aft by 1.9° and preconed up by 4° . However, the feathering axis was fixed to the hub and did not rotate with the blade.

The lead-lag hinge restraint was provided by elastomeric dampers mounted between the blade grips and damper housing outboard of the lag hinge. The mounting was such that blade lead-lag motions about the hinge resulted in shearing deflections of the damper, producing the restraining forces. The viscoelastic properties of the damper were determined experimentally by the manufacturer and are provided in figure 7 in terms of equivalent hinge stiffness and viscous damping coefficient. Empirical curves and associated parameters are also presented in figure 7. The properties of the damper were selected to provide both a first-inplane frequency ratio of 0.65 and damping which would be sufficient to eliminate ground resonance for nominal support-structure characteristics.

Initially, the blade pushrods were inclined from the vertical. However, it was determined that this configuration resulted in a destabilizing pitch-lag kinematic coupling. (See ref. 7.) Therefore, an intermediate adapter was installed between the swashplate and hub as shown in figure 3. Besides eliminating the unfavorable coupling condition, the adapter allowed for variations of both pitch-flap and pitch-lag coupling in the correct sense to stabilize the rotor further, particularly for inplane motions. This was achieved by changing the upper pushrod attachment points to the adapter ring and by adding a spacer between the upper pushrod and pitch horn.

The model rotor was instrumented with four-arm, strain-gage bridges. Beam and chord bending moments were obtained at 4.0 percent radius on all four hub flexures and at 8.0 percent radius on one hub flexure. The mast torque and lead-lag motions about the hinges on all blades were measured. The instrumented blade feathering oscillations were sensed by a strain-gage leaf flexure across the pitch mechanism. Pushrod axial loads were obtained for two blades. On the instrumented blade, beam and chord bending moments were provided by gages located at 25.0, 37.5, 50.0, and 75.0 percent radius. Blade torsion was measured at 25 and 50 percent radius. Engineering load equivalents were recorded periodically with the loads data by employing precision-shunt calibration resistors for each strain-gage bridge.

The model rotor was designed for Froude scale operation in air at atmospheric pressure by using a full-to-model scale factor of 5. Therefore, compressibility and viscous effects on measured data are not represented. However, static and dynamic deflections are properly simulated, which is important for inplane stability testing. A list of model scale factors is presented in table I. Aeroelastic simulation was achieved by maintaining the ratio of rotor natural frequencies to rotor rotational speed and the advance ratio between the model and full scale.

Model-blade cantilevered mode frequencies were calculated by using a coupled lumped mass analysis, described in reference 8, for 20 blade stations and the rotor structural properties listed in table II. The resulting cantilevered frequencies are presented in table III. With regard to terminology, beam and chord designations refer, respectively, to directions perpendicular and parallel to blade planform in the local axis system. In figures 8 and 9 the normalized mode shapes and bending-moment distributions are shown for both beam and chord directions. The two lowest mode shapes indicate that the beam and chord virtual hinges are located at about 8 and 10 percent radius, respectively. The beam moment distributions all decrease from the root to the flexure virtual hinge at 8 percent radius. The second and third modes indicate peak moments near 25 percent radius, and the third mode has another peak near 75 percent radius. The chord moments decrease from the root to the lag hinge with the moment associated with the second mode peaking at approximately 46 percent radius.

Experimental Procedure

The experimental investigation consisted of three separate parts. The first two parts involved wind-tunnel tests of the model to obtain a large volume of data pertaining to the rotor dynamic response and air-resonance stability encountered in forward flight. The third part involved hovering inplane-stability tests to demonstrate freedom from ground resonance and to examine the separate effects of pitch-lag and pitch-flap coupling, pylon stiffness, and rotor thrust on inplane stability. The first part was conducted to study parametrically variations in performance and dynamic-response characteristics with operating conditions. Data were obtained over a large range of the operational parameters (i.e., shaft angle, collective pitch, and forward-flight speed). Throughout this portion of the test the rotor first harmonic out-of-plane moments at the root (4 percent radius) were zeroed out, or, in other words, the rotor was trimmed to shaft. The second part of the investigation was concerned with model simulation runs where the emphasis was on achieving specific model lift and drag forces corresponding to scaled 1g level flight. At each flight speed the operating parameters were generally kept within a narrow range and the first harmonic flapping of the rotor was allowed to vary about the trimmed-to-shaft condition. All testing was conducted in air at atmospheric pressure. Specific test procedures are discussed in the subsequent paragraphs.

Forward-flight parametric study. - Each tunnel run was initiated by setting the collective pitch to a low value which would result in a slight positive thrust in forward flight, bringing the rotor speed up to the proper value, and pitching the model nose-down to an initial value of -5° . The tunnel was then started and the preselected free-stream speed was established. From this point collective pitch was increased, generally by 2° increments, until cyclic control limits were reached or excessive blade loads were

encountered. After the collective sweep was concluded, the collective pitch was returned to the original setting and the shaft angle was changed to the next desired value where the collective sweep was repeated. After data were recorded for all combinations of shaft angle and collective pitch, the tunnel speed was increased to the next desired condition and the process was continued. This procedure was followed until the rotor test envelope had been sufficiently covered. Throughout this portion of the test the first harmonic flapping of the rotor was maintained at the trimmed-to-shaft condition. The model test envelope is plotted in figure 10. The maximum and minimum values of rotor lift coefficient achieved for each combination of shaft angle and advance ratio are identified. Figure 10 indicates that scaled maneuver lift conditions were achieved during the tests. The velocities at which the data are plotted are model values where the simulated values are 2.24 times higher. Thus, the maximum simulated full-scale velocity achieved was 98.8 m/s.

Forward-flight simulation tests.- At each tunnel velocity the model collective pitch and shaft angle were set to predetermined values which would produce a scaled 1g lift when the first harmonic flapping was trimmed to shaft. Table IV lists the simulation values of collective pitch and shaft angle which were calculated by using a rotorcraft-simulation program (refs. 9 and 10). The longitudinal cyclic pitch was then increased and decreased by $1/2^{\circ}$ increments about the initial setting while the collective pitch was used to hold lift constant. This technique provided data at approximately equal lift but with varying drag forces which would represent several fuselage drag areas or auxiliary-propulsion capabilities. After completion of the longitudinal cyclic sweeps the rotor was reset to the initial collective pitch and trimmed-to-shaft conditions. The lead-lag stability at this point was checked by exciting the rotor at the lead-lag mode frequency. Finally, while holding the rotor controls fixed with respect to the shaft, the shaft was stepped nose-up by 1° increments to obtain hub pitching-moment variations with shaft angle.

During the forward-flight tests rotor performance and dynamic response were recorded at each combination of collective and cyclic pitch, shaft angle, and tunnel speed. The tunnel operating conditions, balance data, and model-control settings were recorded on punched cards. The rotor-response data, which were measured by strain gages, were recorded on magnetic tape. Similarly, the fore-and-aft, lateral, and vertical accelerations on the fuselage, balance readings, control settings, and one-per-rev rotor pulse were recorded on tape.

Rotor performance data were calculated by a digital computer program using the TDT data acquisition system in an off-line mode. Adjustments to the balance data were made to remove dead weight and fuselage aerodynamic effects and balance interactions. The data were translated from the balance centroid to the hub. The wind-fixed lift and

drag coefficients normalized by rotor solidity were computed. The data were then rotated into the shaft axis system to determine normalized thrust and propulsion force coefficients, the shaft torque coefficient, and power. The control settings were also printed out in engineering units.

The rotor loads and response were determined by using another digital computer program. The data recorded on magnetic tapes were played back through the analog-to-digital system as part of the TDT data acquisition system. Two seconds of data from each channel were digitized at a rate of 1000 samples per second. The digital data thus formed were processed to yield values of mean and oscillatory loads. A discrete Fourier analysis was carried out to produce response harmonic amplitudes. Shunt calibration signals recorded on tape enable all data to be converted to engineering units prior to the final printout.

Hover inplane stability tests.- During the inplane stability tests of the Flexhinge model rotor, two different pylon support-stiffness conditions were employed. In one case the support stiffness was made as high as possible by replacing the mount springs with steel rods to achieve a dynamically decoupled rotor and fuselage. Tests on this system were made to study "blades only" characteristics. For the second support system the steel rods were removed and replaced by springs which resulted in a much softer GRAM support system. The purpose of these tests was to ascertain the effects of hub motion on rotor stability. Basic characteristics of the GRAM configured in each manner were determined experimentally and are presented in table V.

As discussed previously, the kinematic pitch-lag and pitch-flap coupling of the rotor could be altered. The nominal configuration under study had only minimal built-in pitch-lag kinematic coupling of -0.1° lag back per degree of pitch up. However, hover stability characteristics of two additional configurations were examined. The pushrod attachment point to the intermediate adapter between the swashplate and rotor could be moved radially out from the rotor center line. (See fig. 3.) This caused an inward inclination of the pushrod with a resulting kinematic pitch-lag coupling of -0.32 . By using the original attachment point on the adapter but adding a spacer between the pitch horn and upper end of the pushrod, a combination of kinematic pitch-lag coupling of -0.2 deg/deg and $\delta_3 = 13^{\circ}$ could be established. Lead-lag mode damping and frequency characteristics were determined for all three configurations.

The experimental studies of rotor inplane stability in hover and forward flight were conducted by exciting the rotor through the GRAM control system in a manner which simulated a pilot-induced sinusoidal stick input at a selected amplitude. The frequency of the motion was changed until a condition of response amplitude resonance was obtained. The excitation was then reapplied for a fixed number of cycles at the resonant frequency and the "stick" was brought back to its initial trim condition. The resulting transient

response was analyzed, by using the technique described in reference 11, to determine the frequency and damping associated with the mode of interest.

RESULTS AND DISCUSSION

Hover and Forward-Flight Performance

Figure 11 illustrates performance data measured during hover. The data are plotted in terms of torque and thrust coefficients normalized by rotor solidity. Figure 12 illustrates variations in forward-flight performance for advance ratios of 0.22, 0.30, 0.35, 0.40, and 0.45. In each figure the torque and thrust data are presented, when available, for shaft angles of 5° , 0° , -5° , -10° , and -15° . The data in these figures exhibit uniform trends. Figure 13 presents variations of normalized lift and drag coefficients with shaft angle, collective pitch, and advance ratio. Since these data pertain to a powered rotor, the measured drag is negative for some operating conditions. The data of figure 13 can be used to make approximate predictions of shaft-angle requirements for various conditions of gross weight and fuselage drag area. From the lift, drag, and shaft-angle information, the data of figure 12 can be employed to determine the power required. All of the data presented in figures 11 to 13 were obtained from the parametric study where the rotor was always trimmed to shaft.

Measured Rotor-Response Trends

Spanwise distributions of oscillatory bending moments for both beam and chord directions are presented in figures 14 to 16. The oscillatory moments are equal to one-half of the peak-to-peak values of the dynamic response. These figures illustrate spanwise moment distributions for varying shaft angles, advance ratios, and rotor lift and drag. The characteristic drop in both beam and chord moments from the root to the virtual hinges is evident. The beamwise virtual hinge is at 8 percent radius, and the lead-lag hinge is at 10 percent radius. The measured beam oscillatory moments peak near 25 percent radius and then diminish toward midspan. A second minor peak in beam moments occurs at approximately 75 percent radius with the moments becoming zero at the tip. The chord moments peak outboard of the lead-lag hinge before dropping to zero at the tip. As illustrated in these figures the basic character of the beam and chord moment distributions is unaffected by variations in the operating state. However, the maximum oscillatory beam moments shown in figure 14 were measured at 25 percent radius, whereas those in figures 15 and 16 occurred at the blade root. The data of figure 14 result from the parametric tests, where the first harmonic flapping of the rotor was trimmed to shaft, whereas the data of figures 15 and 16 are from simulation cases. Thus, it is evident that the relative magnitudes of the beam moments along part of the blade radius depend on the degree of flapping involved.

As mentioned previously, wind-tunnel tests were conducted under two distinct sets of guidelines. For the parametric tests the rotor was maintained at a trim-to-shaft condition which is the most expedient technique for collecting data. Such a restraint does not detract from observations drawn with regard to parametric variations. However, in the "real world" of helicopter operations the first harmonic flapping of the rotor is rarely zero and may vary up to several degrees. Therefore, if the intent is to correlate with full-scale load measurements or to provide a prediction of rotor loads that would be encountered on flight hardware, such a test plan may not be proper. As an illustration, figure 17 presents trends of hub (4 percent radius) oscillatory and harmonic-moment amplitudes with changes in longitudinal cyclic-trim condition. The harmonic moments are the total amplitudes of the components of response at integral multiples of the rotor rotational speed. The beam moments vary significantly with changes in trim condition, primarily due to the change in one-per-rev airloads. The same is true for the chordwise direction except for a difference of magnitude. For 2° of cycle change from trim, the oscillatory beam moments increase by a factor of almost 4, and the chord moments vary by more than 15 percent (figs. 17(a) and 17(b), respectively). The higher harmonic moments are not as significantly affected by trim state. In figure 18, the trends of blade moments (25 percent radius) are similar, although not as large. In summary, the magnitude of the oscillatory and one-per-rev harmonic moments on the rotor can vary significantly with rotor trim. From comparing figures 17 and 18 it is evident that the sensitivity of the moments to trim diminishes for stations further out on the blade.

Spanwise distributions of all significant harmonic amplitudes in beam and chord directions are plotted in figure 19. For the beam moments the first harmonic component is approximately 80 percent of the oscillatory in the root area. At the 25-percent-radius station the third harmonic becomes greater than the first with significant amounts of second and fifth harmonics present. At the outboard station the largest harmonic is due to two-per-rev airloads. The first harmonic moments result from the action of one-per-rev forces exciting the lowest flexible beam mode. The distribution of first harmonic response resembles the first flexible beam-mode moment. The second and third harmonic moments arise from the second flexible beam mode and have distributions similar to the second mode-moment curve in figure 9(a). Similarly, the fifth harmonic response is associated with the third flexible beam mode and is similar in spanwise characteristics. Over one-half of the oscillatory chord moments in figure 19(b) are due to 1P airloads and the first flexible chord mode. (1P represents 1 cycle of response per revolution of the rotor blade.) The 1P harmonic-moment distribution and that of figure 9(b) for the first inplane mode are very similar in character. As shown in table III, the second flexible chord mode occurs at a frequency ratio of 5.69, well above the

frequencies of the 2P and 3P responses. Thus, the significance of the 2P and 3P chord moment is due to response in the beam direction and the coupling of the beam and chord mode shapes in the second beam mode.

Variations of oscillatory and harmonic components with lift are presented in figure 20. These data were collected from tests where the first harmonic flapping was trimmed to shaft. However, this should not bear significantly on the subsequent discussion of data trends. The responses selected for illustration include beam and chord moments at 4 and 25 percent radius, torsion moments at 50 percent radius, pushrod load, and lead-lag motions about the hinge. Both oscillatory and harmonic loads increase sharply with lift, particularly at the higher lift values. From figure 20 the largest harmonic loads forming the overall response can be easily identified. At the higher lifts the 2P and 3P beam moments are larger than any higher harmonic, and the 1P component dominates the chord moments. The 1P and 2P harmonics are the most significant contributors to the torsional moments and control loads plotted in figures 20(e) and (f). In figure 20(g) the variation in blade mean lead-lag angle about the hinge is given and includes the 1.9° aft sweep built into the rotor hub. The sweep serves to diminish the inplane steady-state hub stresses due to blade drag and corresponds approximately to the blade mean lag angle at cruise-power conditions and moderate advance ratios. The mean lag angle begins to increase sharply as C_L/σ surpasses a value of 0.06. The oscillatory lead-lag motion about the hinge is composed almost entirely of 1P response, especially at the higher lift conditions.

The rotor forces required to maintain level flight for the simulated vehicle are illustrated in figure 21 as a function of advance ratio. The data were calculated by assuming a hover C_L/σ of 0.06 (66.7 kN (15 000 lbf)) and an equivalent frontal flat-plate drag area of 1.6 m^2 (17 ft^2). The symbols in figure 21 represent performance conditions associated with five data points with the associated trim conditions listed in table IV. Figure 22 presents the measured oscillatory and harmonic responses for those test points. The channels selected for illustration include beam and chord moments at 4 and 25 percent radius, torsion moments at 50 percent radius, pushrod loads, and the motion about the lag hinge. The beam and chord root moments are mostly responses due to the 1P airloads. The beam moment also has significant amounts of 2P and 3P response and the chord has a large 3P harmonic. On the blade the 2P and 3P harmonics are significant components in the beam direction, and the 1P harmonic is most significant in the chord direction. For the torsion and pushrod loads, the 1P component is dominant at low advance ratios but decreases in importance relative to the 2P values at the higher advance ratio. The variation of mean lag angle with μ is very similar to the change with lift with a greater rate of increase at the higher μ values. The 1P harmonic lag angle represents 80 percent of the total oscillatory level at $\mu = 0.45$. Some 3P lagging

is present as shown in figure 22(h). The maximum lead-lag excursion observed was only $\pm 1.62^\circ$ at the highest advance ratio where the steady-state angle was approximately 4.3° . The rotor loads and response were all within acceptable limits throughout the test envelope, and no adverse response characteristics were encountered. The rotor modes were generally well separated from the n-per-rev resonance lines, and no harmonic-load amplification problems were observed. The maximum measured bending moments were incurred at 4 percent radius and were 13.6 N-m (120.4 in-lb) and 22.3 N-m (197.4 in-lb) for the beam and chord directions, respectively.

The rotor-hub moment trends are plotted in figures 23 and 24. The data in figure 23 were obtained by applying cyclic pitch to the rotor in hover and determining the steady hub moments from the six-component balance recordings. As noted earlier in this report, one of the favorable characteristics of the hingeless rotor is its capability to transmit moments from the blades to the hub and thus to the fuselage. This hub moment augments control moments resulting from tilting the thrust vector and provides increased control power. The data of figure 23 include three thrust levels. Of significance is the amount of hub moment available for helicopter control even for the nearly zero thrust condition, where the measured rate was about 10.0 N-m (88.5 in-lb) per degree of cyclic pitch. In figure 24 the rotor pitch and roll moment with shaft-angle derivatives are plotted for advance ratios up to 0.45. Although the rotor is soft out of plane, moderate coupling between the pitch and roll directions occurs. Proper selection of control phase angle and pitch-flap coupling can be used to eliminate much of the $C_{l\alpha}$ effect.

Inplane Dynamic Stability

Figure 25 presents the fixed-system pylon and blade frequencies at a rotational speed of 64.4 rad/s. The blade data are calculated by using the characteristics of figure 7 and a Southwell coefficient of 0.189 obtained from the lumped-mass analysis used to generate the data of table III. The pylon data result from the characteristics of table V and were verified experimentally. As shown in figure 25, the resonance frequencies of the soft pylon and blade lead-lag modes tend to merge for small values of lead-lag motion. During tests on the soft pylon, excitation of the blade lead-lag mode resulted in considerable hub motion even for the higher lead-lag amplitudes. On the stiff pylon, hub motions were minimal and the resulting blade trends should be relatively unaffected by support-system properties.

Figures 26 to 30 present a summary of the results of the inplane hover stability tests of the Flexhinge rotor. The data were measured during hover and resulted from application of a constant 2° of forward (in the direction of rotor rotation) stick-stir excitation at the resonance frequencies. During the tests of each configuration collective

pitch was varied to achieve a range of thrust C_T/σ from almost 0 up to a value of 0.06. The data are presented in these figures as variations with the sustained lead-lag response amplitude of motion (figs. 26 to 28) or with thrust level (figs. 29 and 30).

The variation of lead-lag mode frequency (in the rotating system) is illustrated in figures 26 and 27 for the stiff and soft-pylon support systems, respectively. The normalized frequency in the rotating system decreased with amplitude but remained between 0.6 and 0.7 for all significant amplitudes of lead-lag motion (above 0.4°). The trends did not vary significantly with changes in hub impedance or kinematic coupling introduced into the hub. Although the lead-lag frequency does vary slightly with operating conditions and configuration, the placement remains close to the design value of 0.65 and does not change enough to create any significant problems in design or during operation. For comparison the empirical rotating-frequency characteristics (based on the data in fig. 7) are included in both figures 26 and 27 and reflect the contributions from the damper only.

In figure 28 the measured lead-lag mode damping for the rotor mounted on the stiff pylon is shown along with the empirically derived characteristics. The basic elastomeric damper characteristics are such that the equivalent hinge damping ratio decreased with amplitude. However, the measured damping ratio increases with motion due to the contributions from aerodynamic sources and elastic pitch-flap-lag coupling as discussed in reference 3. The Flexhinge rotor has coupling between the flap and lag directions due to the blade twist and feathering of the lag hinge axis. This inherent flap-lag coupling leads to inplane damping contributions from the aerodynamic flap damping which is very large. The first out-of-plane mode shape (fig. 8(a)) indicates that a significant amount of the elastic deflection of the blade occurs in the root (flexure) area. Since the feathering bearings are located outboard of the flapping flexures, relative deflections between the blade and feathering axis are reduced. However, elastic pitch-lag coupling, although reduced, is still present. Further, the elastic pitch flap in the presence of inherent flap-lag coupling can form an additional source of pitch-lag coupling with its beneficial effects.

In figure 29, the data of figure 28 are replotted in terms of the corresponding rotor thrust. The damping ratio first decreases slightly and then increases with thrust up to the maximum test value of C_T/σ of 0.06 (simulated 1g lift). This trend is due to variations in the equivalent pitch-lag coupling as shown in reference 3 which is sensitive to blade elastic deflections and thus to the lift. As shown in figure 29, the kinematic coupling that was built into the hub, in excess of the nominal value, contributed a damping increment of approximately 0.02 throughout the lift range. In figure 30, the damping trends are plotted for the rotor mounted on the soft pylon. The beneficial effect of thrust may diminish slightly due to pylon motion, but no significant loss of damping for the lead-lag mode was observed. Even though the soft pylon had an inherent damping ratio

of 0.034 and 0.043 and was in a near-resonance condition with the rotor, no ground-resonance instabilities occurred due to the fact that the inplane damping ratio remained above 8 percent. Figure 31 illustrates the variation of rotor air-resonance stability with advance ratio. Although the minimum value was less than that observed during hover, the measured damping ratio still remained above 0.05.

CONCLUDING REMARKS

An experimental investigation has been conducted of the dynamic response and blade inplane stability associated with a new soft-inplane four-blade main rotor system. The rotor design incorporated a blade lead-lag hinge with hinge restraint and damping provided by an internal elastomeric damper. The properties of the elastomer were selected to achieve both a nominal first inplane frequency ratio of about 0.65 and sufficient damping to preclude ground resonance for typical fuselage structures. Out-of-plane characteristics were based on soft flexures near the hub which were designed to achieve a virtual hinge location of 8 percent radius and a first mode frequency ratio of 1.06. For the investigation a 1/5-scale aeroelastic model was used to represent the rotor. The model blades had an NACA 0012 airfoil. The model diameter was 3.05 (10 ft) with a solidity of 0.103.

Rotor performance, loads, and response were measured for a large array of operating conditions. The forward-flight tests covered advance ratios up to 0.45, thrusts up through simulated maneuver values, and various trim conditions. The rotor loads and response encountered in forward flight proved to be acceptable throughout the test envelope. Generally, both beam and chord oscillatory bending moments were highest near the rotor center with measured values at 4 percent radius reaching 13.6 N-m (120.4 in-lb) and 22.3 N-m (197.4 in-lb), respectively. Oscillatory lead-lag excursions about the hinge did not exceed 1.62° for unaccelerated level flight. One characteristic of this design was the large moments transmitted from the blades to the hub which improved the control power. These moments occurred even for cases of almost zero thrust in hover, where the control moment was 10.0 N-m (88.5 in-lb) per degree of cyclic pitch. During the testing no adverse characteristics of this rotor concept were observed.

The investigation included blade inplane-stability testing in hover by using sinusoidal excitations applied through the swashplate simulating "pilot-induced oscillations." Due to the properties of the elastomeric damper, slight variations in lead-lag frequency occurred with changes in thrust. However, even with this variation the frequency ratio remained close enough to the design value of 0.65 that no unexpected problems were encountered. The lead-lag damping ratio exceeded a value of 0.08 for all conditions in hover and increased to higher levels as the thrust reached 1g values. Kinematic pitch-lag

coupling built into the hub added an additional damping increment of up to 0.02 to the system. The rotor was stable even when mounted on a soft pylon having damping ratios of 0.03 and 0.04 and considerable coupling between the pylon and blade lead-lag modes. In forward flight the first-inplane mode damping ratio was slightly lower, but remained above 0.05. The rotor simulated a soft-inplane hingeless design with all its merits while providing additional inplane damping over that generally encountered on hingeless rotors without external dampers.

Langley Research Center
National Aeronautics and Space Administration
Hampton, VA 23665
April 14, 1977

REFERENCES

1. Ward, John F.; and Huston, Robert J.: A Summary of Hingeless-Rotor Research at NASA - Langley. Proceedings of the Twentieth Annual National Forum, American Helicopter Soc., Inc., May 1964, pp. 76-83.
2. Hohenemser, Kurt H.: Hingeless Rotorcraft Flight Dynamics. AGARD-AG-197, Sept. 1974.
3. Huber, H. B.: Effect of Torsion-Flap-Lag Coupling on Hingeless Rotor Stability. Preprint No. 731, American Helicopter Soc., May 1973.
4. Ormiston, Robert A.: Techniques for Improving the Stability of Soft Inplane Hingeless Rotors. NASA TM X-62,390, 1974.
5. Lytwyn, R. T.; Miao, W.; and Woitsch, W.: Airborne and Ground Resonance of Hingeless Rotors. Preprint No. 414, American Helicopter Soc., June 1970.
6. Ormiston, R. A.; and Bousman, W. G.: A Study of Stall-Induced Flap-Lag Instability of Hingeless Rotors. Preprint No. 730, American Helicopter Soc., May 1973.
7. Chou, Pei Chi: Pitch-Lag Instability of Helicopter Rotors. J. American Helicopter Soc., vol. 3, no. 3, July 1958, pp. 30-39.
8. Bennett, R. L.: Digital Computer Program DF1758 Fully Coupled Natural Frequencies and Mode Shapes of a Helicopter Rotor Blade. NASA CR-132662, [1975].
9. Davis, John M.; Bennett, Richard L.; and Blankenship, Barney L.: Rotorcraft Flight Simulation With Aeroelastic Rotor and Improved Aerodynamic Representation. Volume I - Engineer's Manual. USAAMRDL TR-74-10A, U.S. Army, June 1974. (Available from DDC as AD 782 854.)
10. Davis, John M.: Rotorcraft Flight Simulation With Aeroelastic Rotor and Improved Aerodynamic Representation. Volume II - User's Manual. USAAMRDL TR-74-10B, U.S. Army, June 1974. (Available from DDC as AD 782 756.)
11. Hammond, Charles E.; and Doggett, Robert V., Jr.: Determination of Subcritical Damping by Moving-Block/Randomdec Applications. Flutter Testing Techniques, NASA SP-415, 1976, pp. 59-76.

TABLE I.- MODEL SCALE FACTORS

Item	Units	Scale factor (a)
Length	m	5
Weight	N	125
Structural stiffness	N-m ²	3125
Angular velocity	rad/s	0.447
Linear velocity	m/s	2.236
Force	N	125
Moment	N-m	625
Power	N-m/s	279.5
Froude number		1.0
Rotor Lock number		1.0
Advance ratio		1.0
Structural frequency ratio		1.0

^aRatio of full scale to model.

TABLE II - STRUCTURAL PROPERTIES OF ROTOR MODEL

Segment	Length, cm	Mass, kg/m	Structural stiffness			Radius of gyration, cm	Chordwise shear center offset, cm (c)	Chordwise center- of-gravity offset, cm (d)
			Beam, N·cm ²	Chord, N·m ²	Torsion, N·m ²			
1	5.08	4.036	576.8	43 906	(b)	0	0	0
2	2.72	.661	12.9	8 466	(b)	0	0	0
3	2.72	.554	5.1	5 768	(b)	0	0	0
4	2.72	.482	3.4	4 333	(b)	0	0	0
5	1.78	.393	54.2	11 020	(b)	0	0	0
6	.51	4.000	127.7	3	(b)	2.00	.005	-.005
7	9.14	6.018	149.8	7 346	108.2	2.20	.036	-.005
8	11.94	1.605	677.2	3 874	122.8	2.37	.127	.024
9	9.65	1.489	309.9	3 645	74.6	1.15	.234	.023
10	9.65	1.418	287.0	3 472	55.7	2.00	.409	.015
11	9.65	.571	27.6	895	49.4	3.02	.569	.013
12	9.65	.429	22.9	887	47.6	3.54	.709	.145
13	9.65	.429	22.9	887	47.6	3.56	.742	.206
14	9.65	.429	22.9	887	47.6	3.56	.742	.206
15	9.65	.429	22.9	887	47.6	3.56	.742	.206
16	9.65	.429	22.9	887	47.6	3.56	.742	.206
17	9.65	.429	22.9	887	47.6	3.56	.742	.206
18	9.65	.429	22.9	887	47.6	3.56	.742	.206
19	9.65	.429	22.9	637	47.6	3.56	.742	.206
20	9.65	.429	22.9	887	47.6	3.56	.742	.206

^aFirst segment starts at rotor center line.^bValues were more than one order of magnitude higher than maximum value shown in column.^cPositive for offset aft of feathering axis (0.25c).^dPositive for offset forward of feathering axis (0.25c).

TABLE III - CALCULATED NATURAL-FREQUENCY
RATIOS OF ROTOR

Frequency ratio (a)	Mode identity
0.68	Chord
1.06	Beam
2.41	Beam
3.40	Torsion
4.64	Beam
5.69	Chord

$$a_{\Omega} = 64.4 \text{ rad/s}; \theta_{0.75R} = 9^0.$$

TABLE IV. - TRIM SCHEDULE OF SIMULATION PROGRAM

Advance ratio	Shaft angle, deg	Collective pitch at 0.75R, deg
0.22	-3.6	7.0
.30	-6.6	9.3
.35	-8.9	11.6
.40	-12.5	15.6
.45	-16.0	20.3

TABLE V.- STRUCTURAL CHARACTERISTICS OF PYLON

Direction	K , N/m	M , kg	C , N-s/m
Soft GRAM support system			
Lateral	7 808	40.86	38.24
Longitudinal	12 507	82.46	86.25
Stiff GRAM support system			
Lateral	157 048	47.0	81.5
Longitudinal	155 123	99.0	431.0

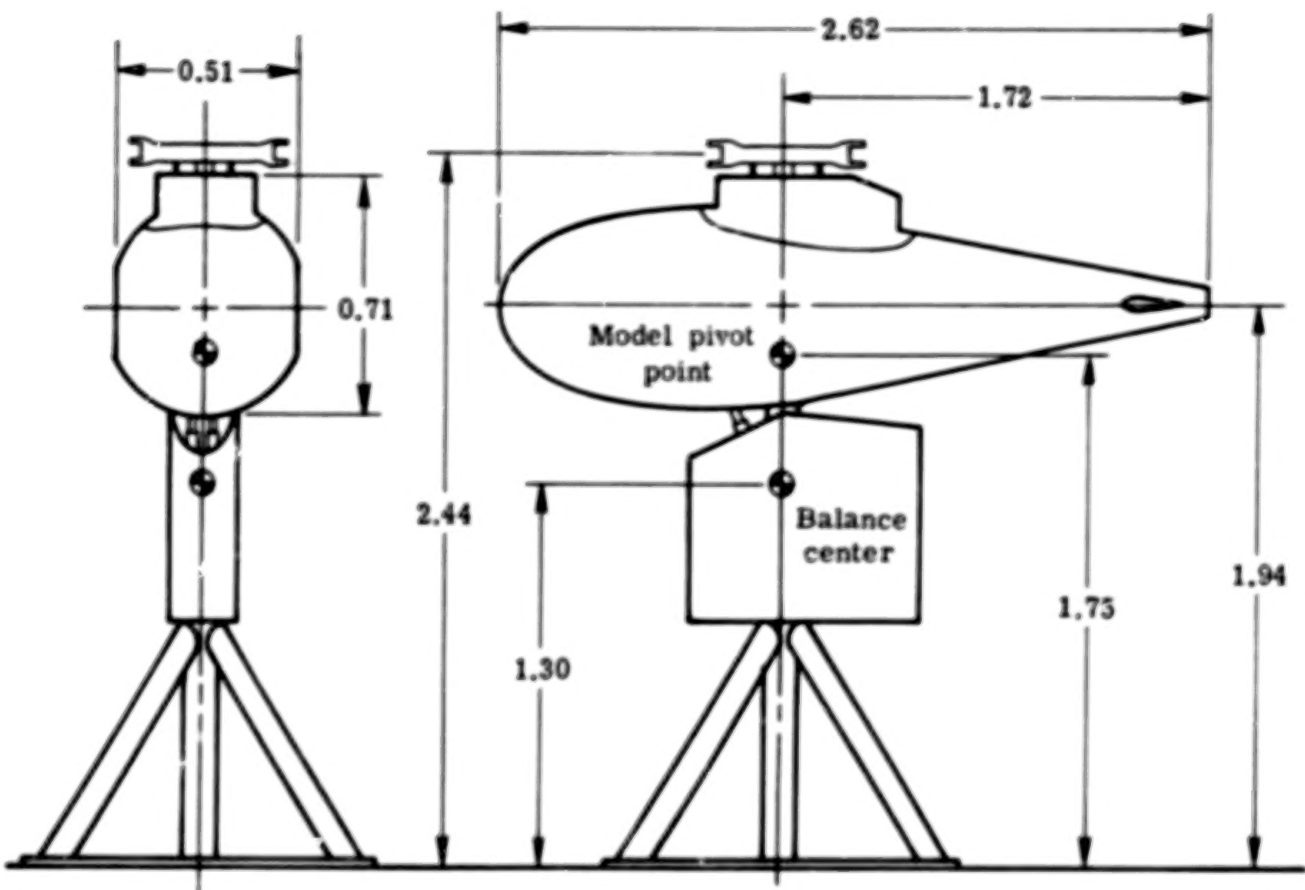
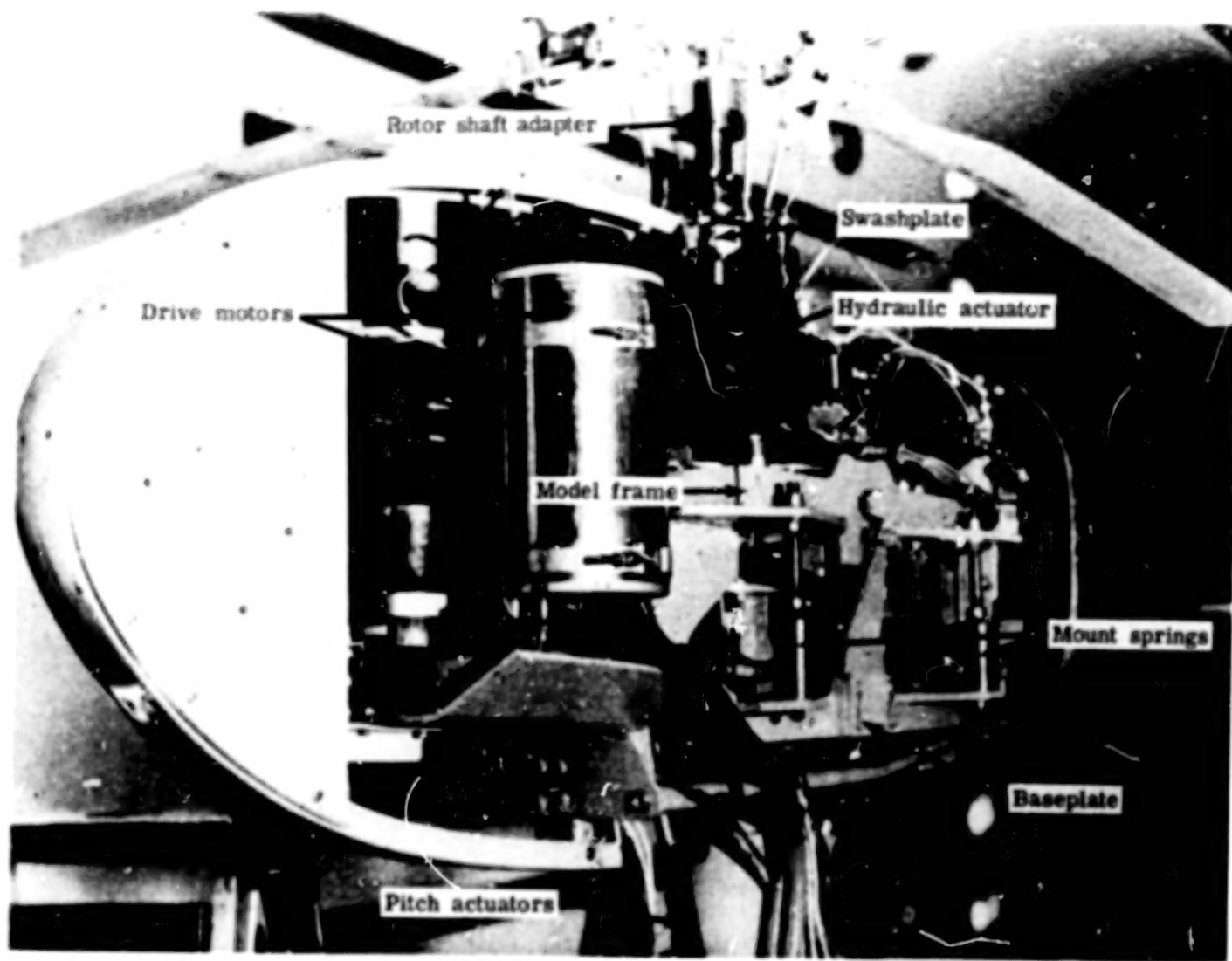


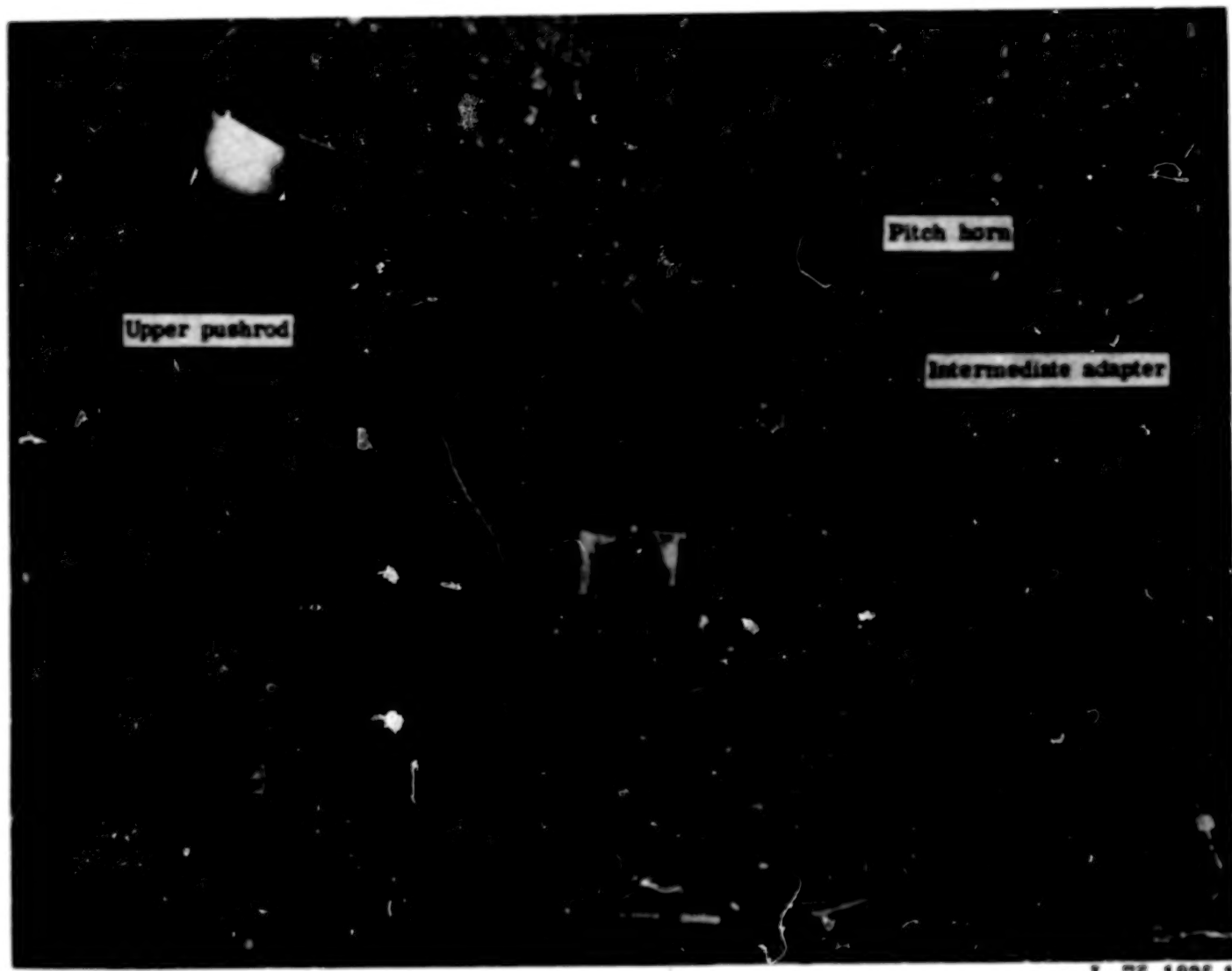
Figure 1.- Schematic diagram of generalized rotor aeroelastic model. All dimensions are given in meters.

23.



L-75-1500.1

Figure 2.- Detailed view of generalized rotor aeroelastic model.



L-75-1825.1

Figure 3. - Control system for generalized rotor aeroelastic model.

25.



26.

Figure 4.- Test model mounted on generalized rotor aeroelastic model.

L-75-1553

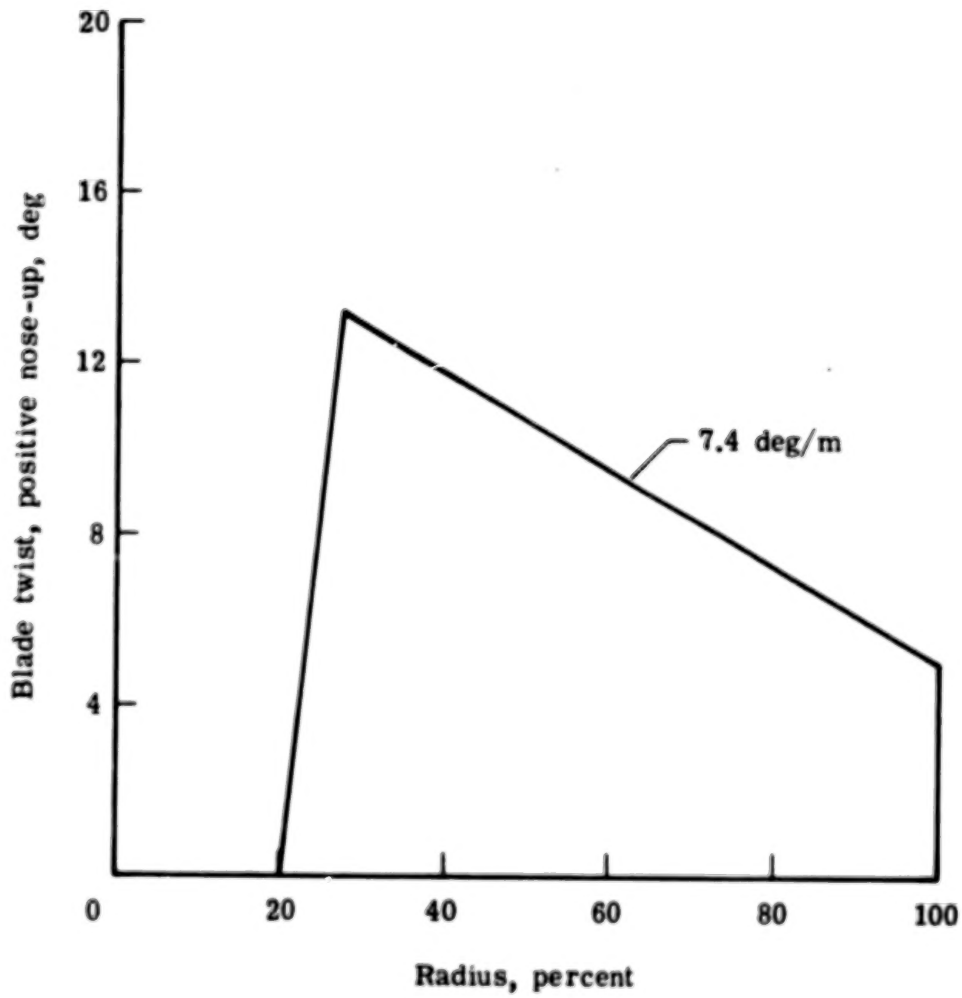
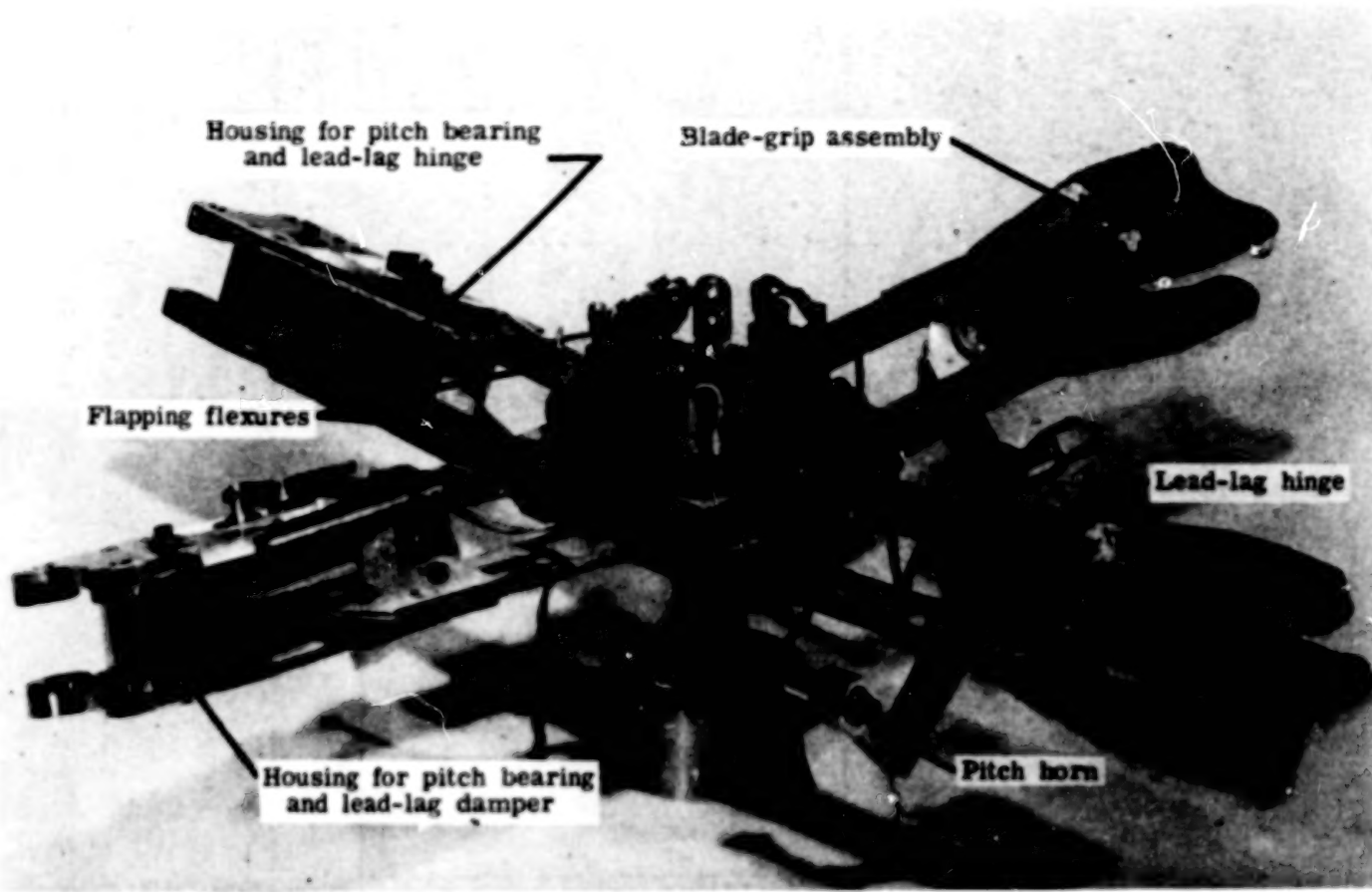


Figure 5.- Twist distribution of model blade.

27,



L-75-732.1

Figure 6.- Details of model rotor hub.

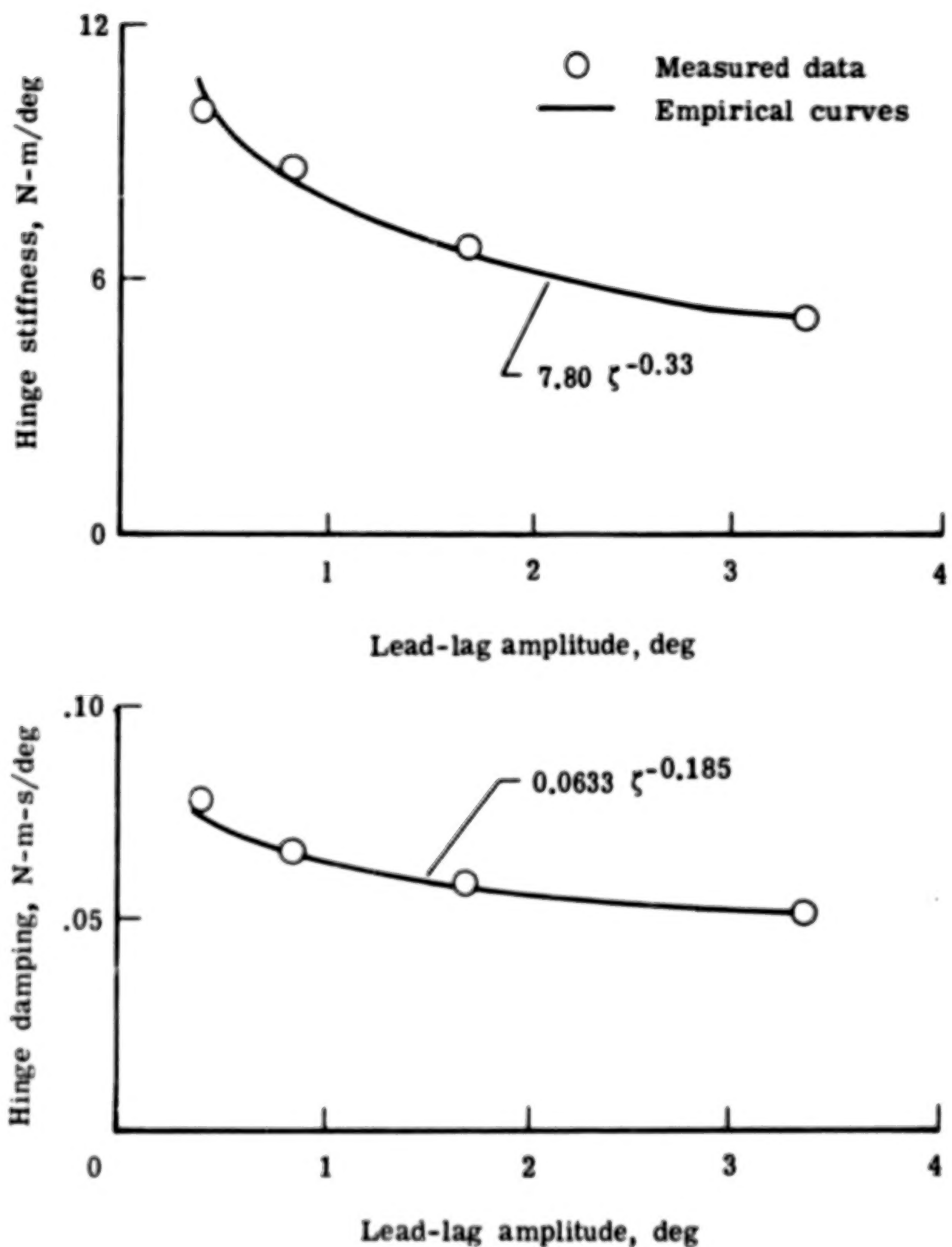
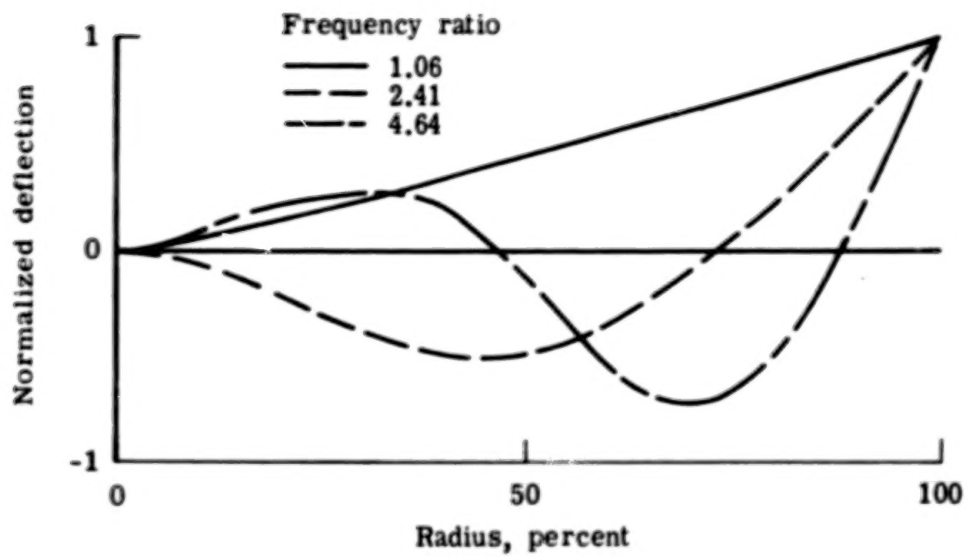
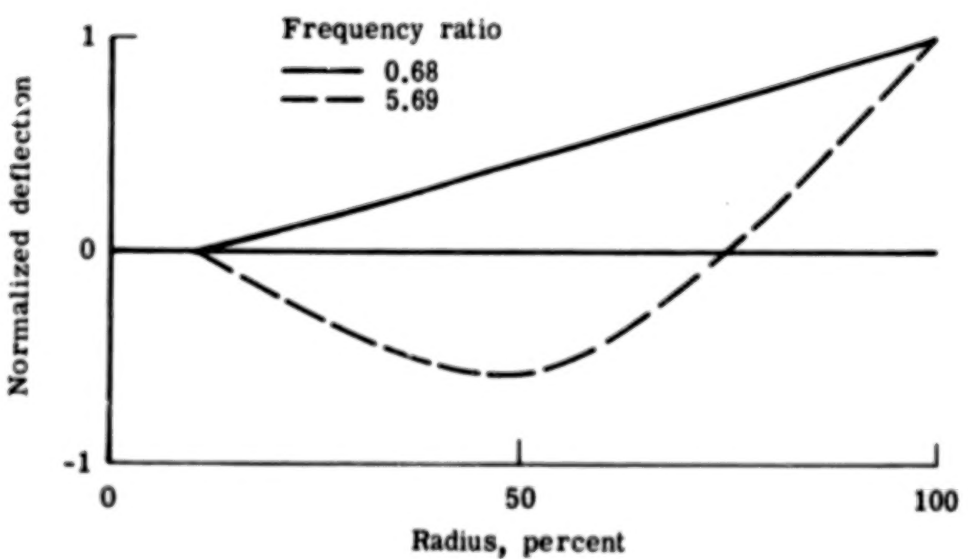


Figure 7.- Measured characteristics of the blade lead-lag damper.
Hinge damping was based on a blade mass moment of inertia of
 $0.394 \text{ kg}\cdot\text{m}^2$.

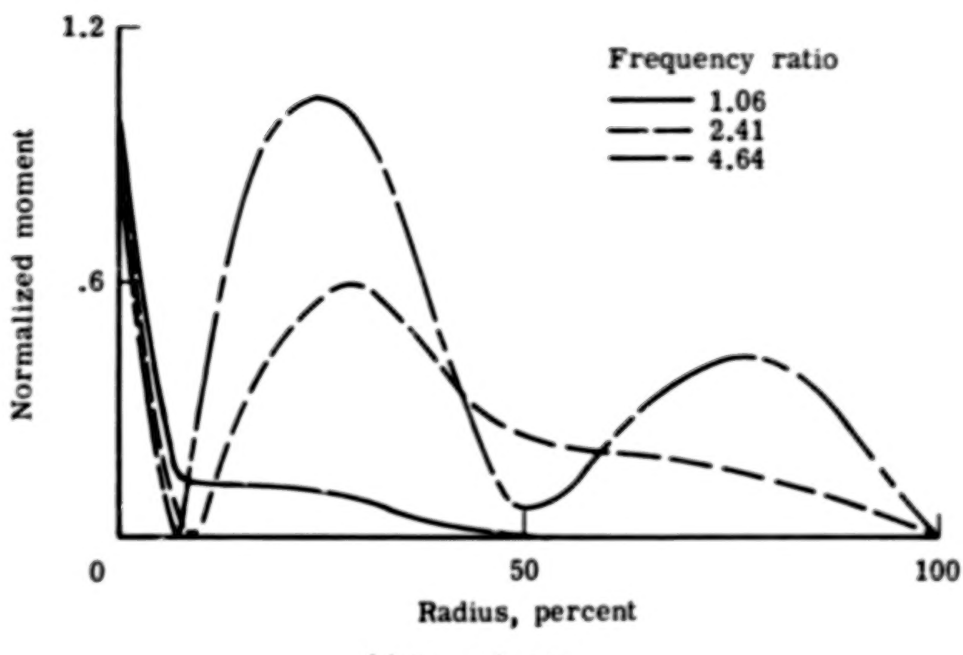


(a) Beam bending.

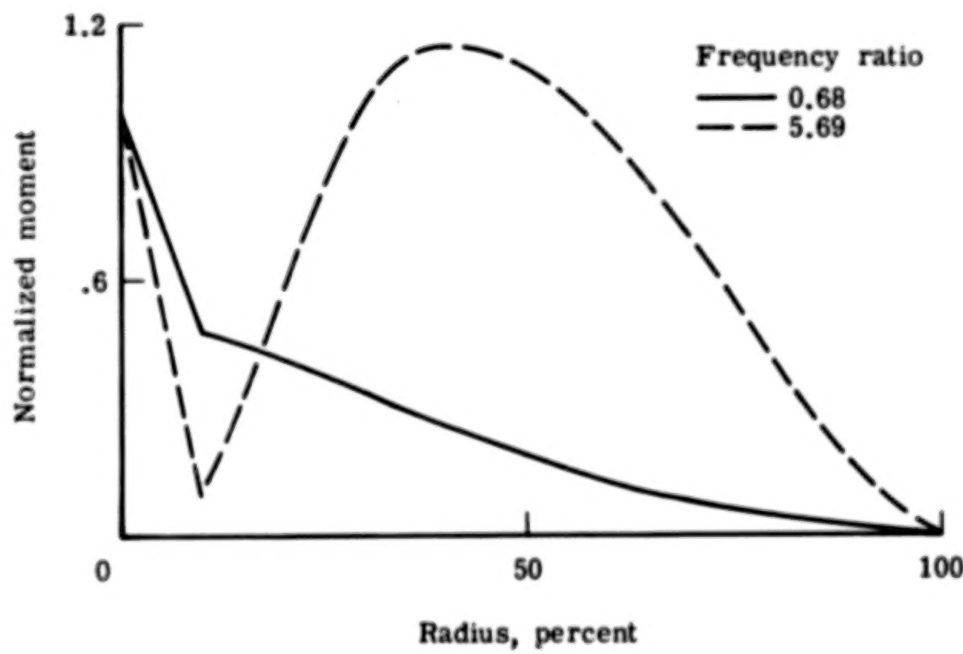


(b) Chord bending.

Figure 8.- Calculated mode shapes of the blade.



(a) Beam bending



(b) Chord bending.

Figure 9.- Calculated moment distributions for the blade modes.

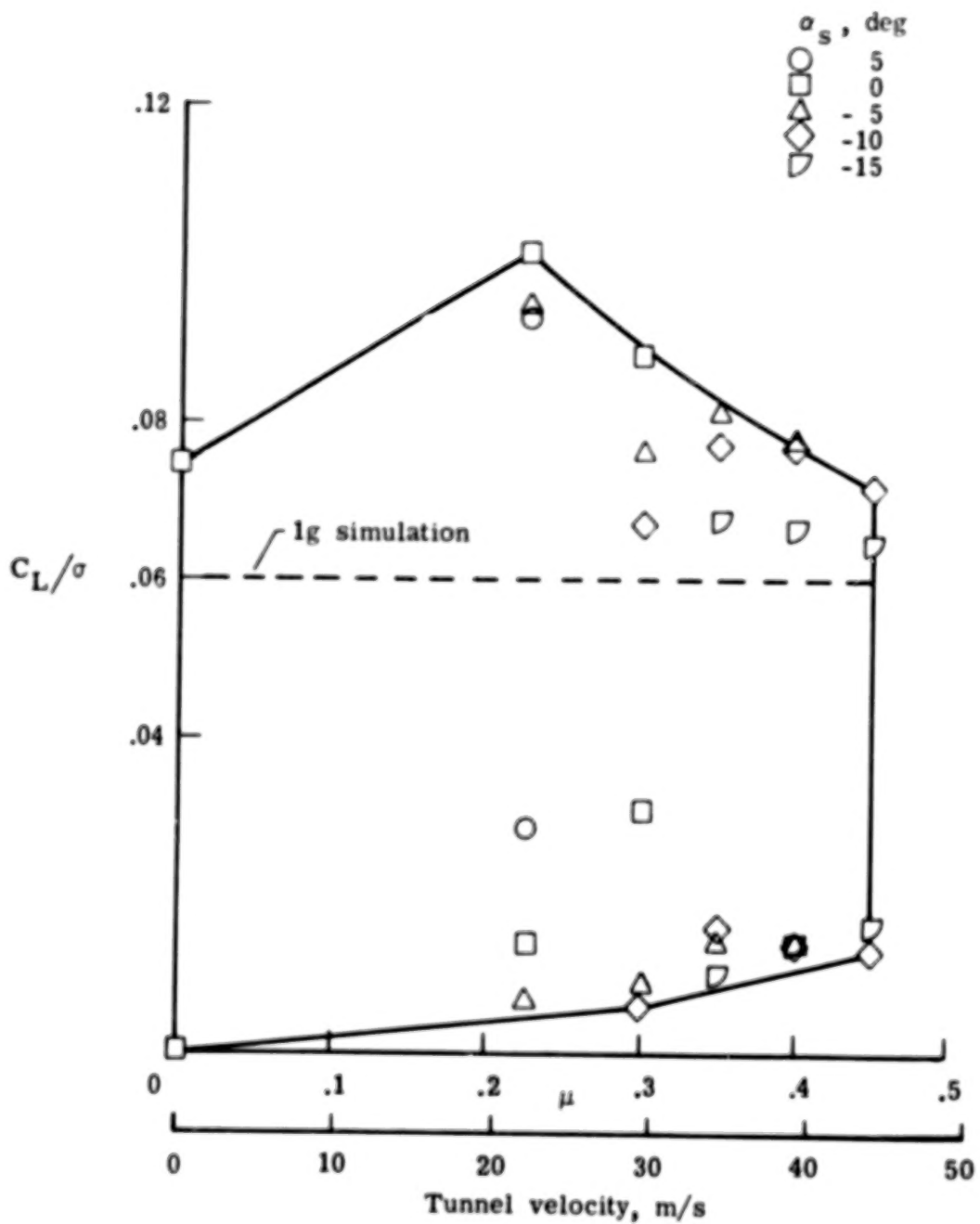


Figure 10.- Envelope of model test conditions.

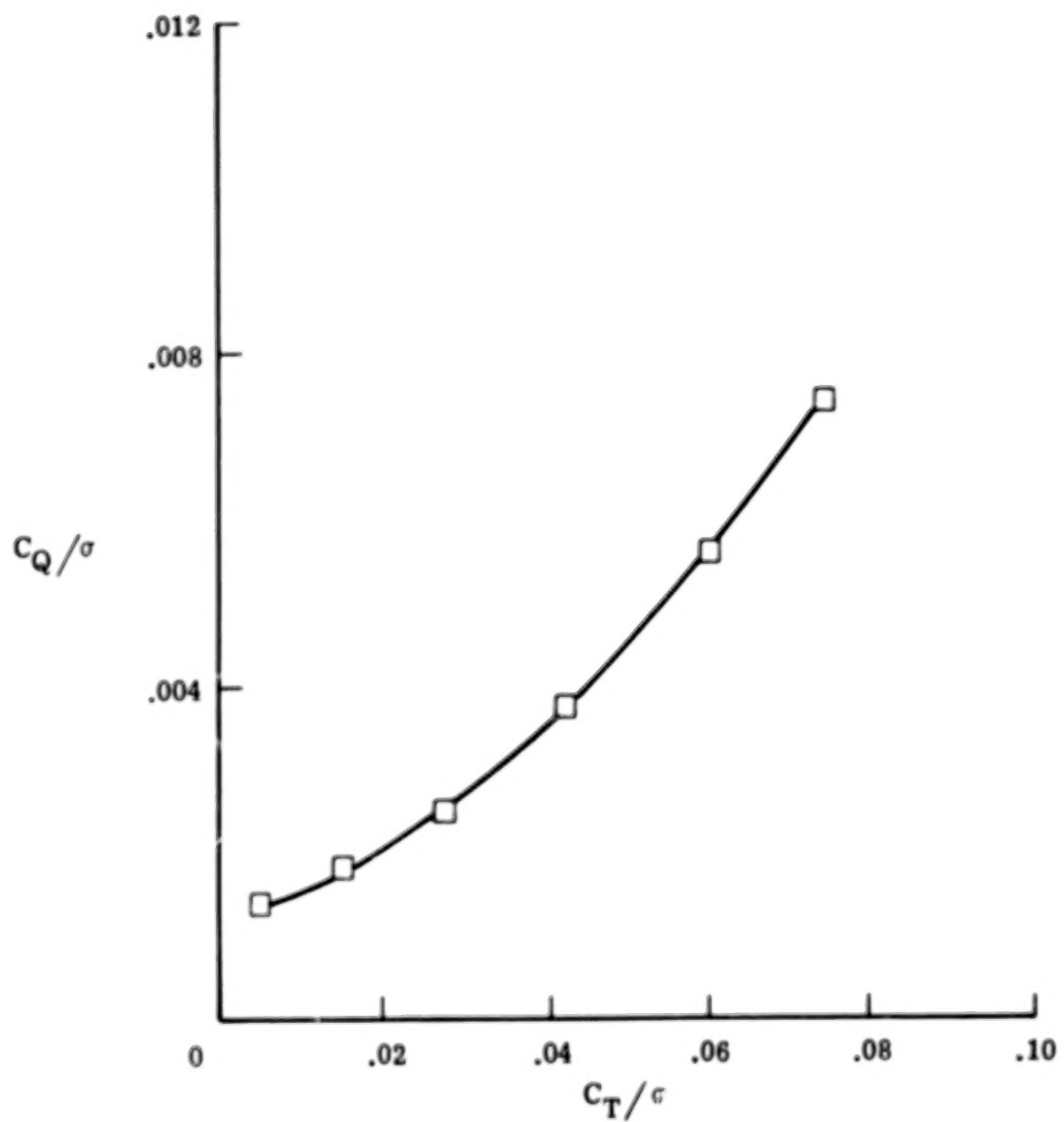
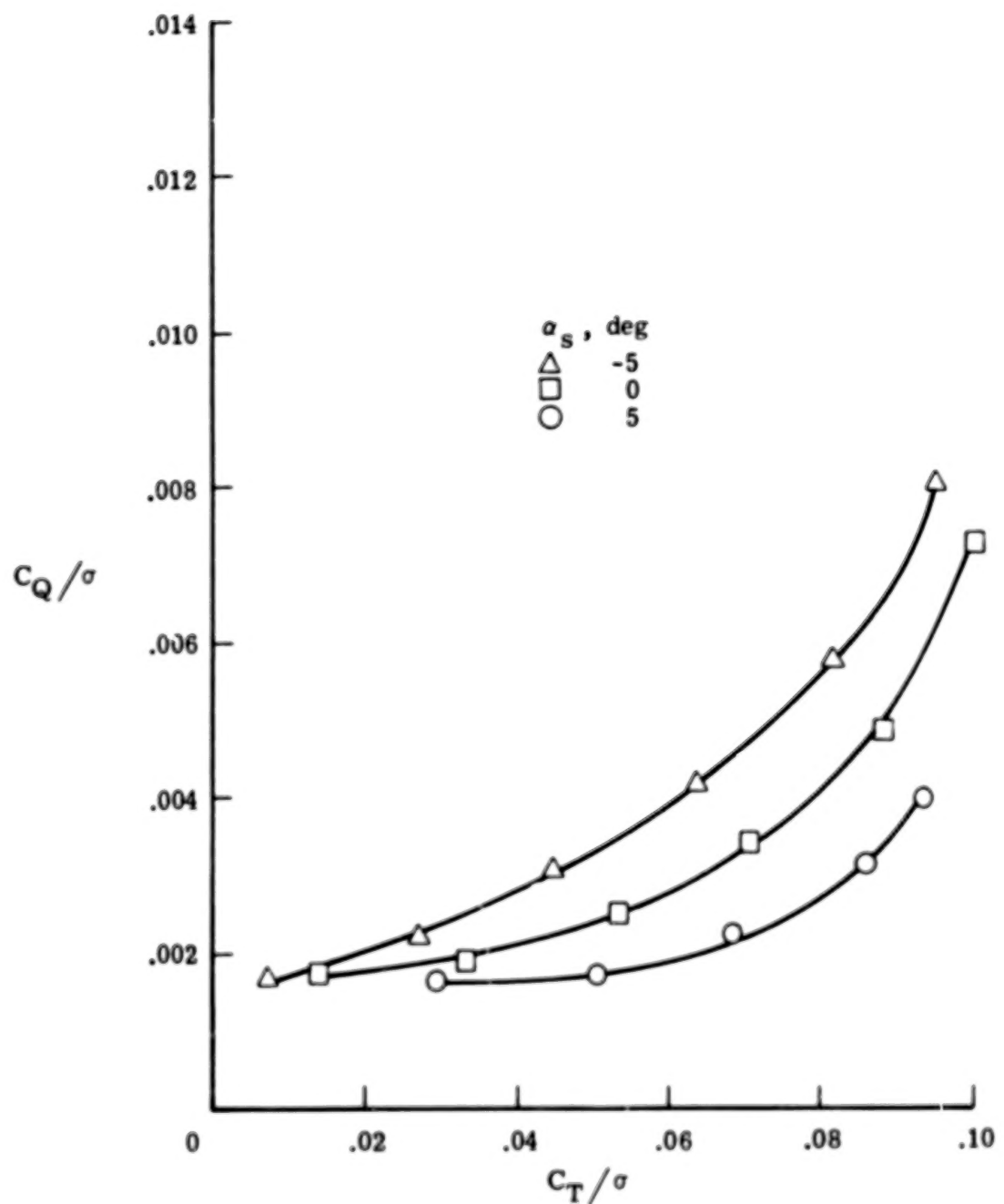


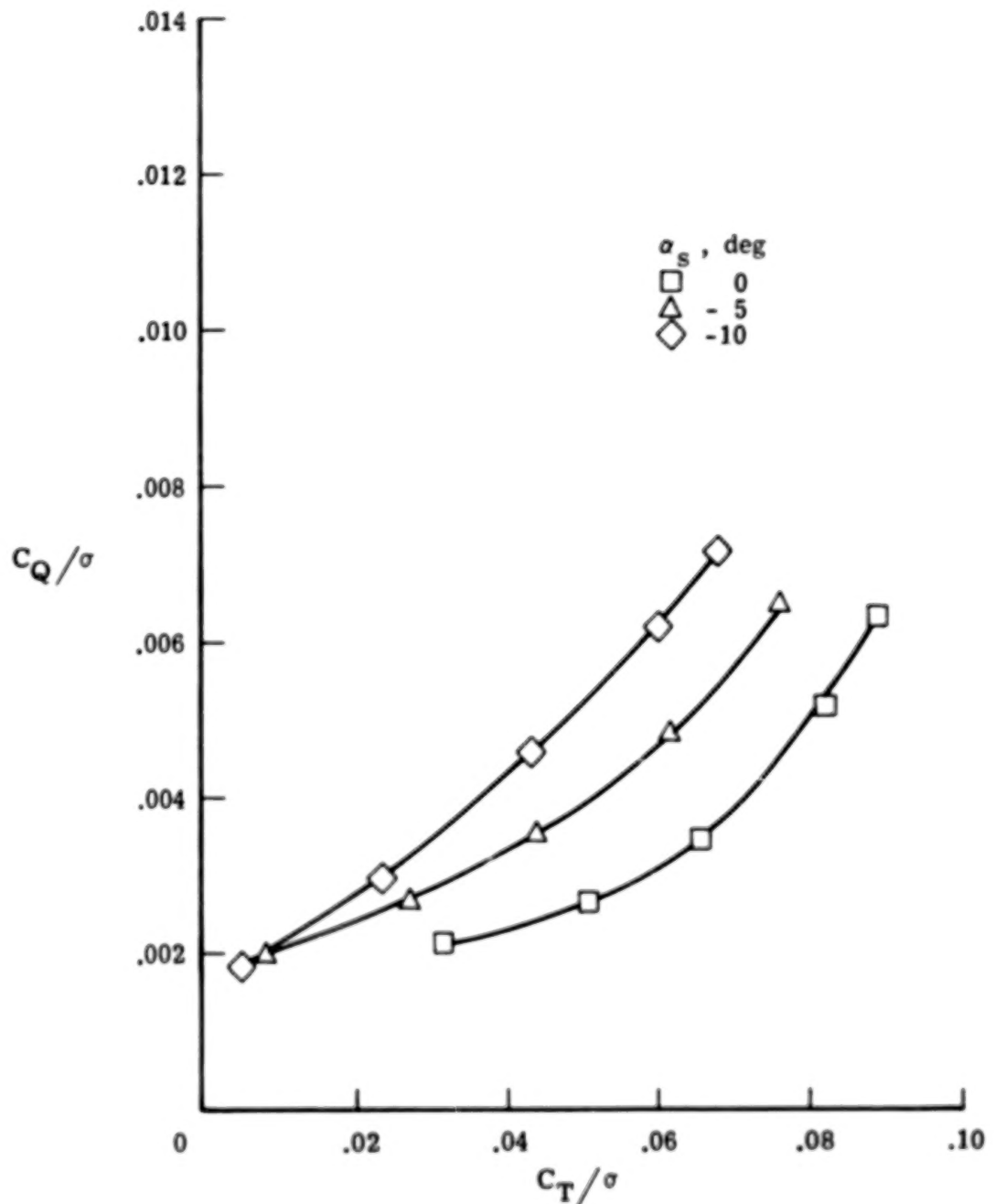
Figure 11.- Variation of rotor torque with thrust for hover.

$$\alpha_s = 0^\circ; \Delta B_1 = 0^\circ.$$



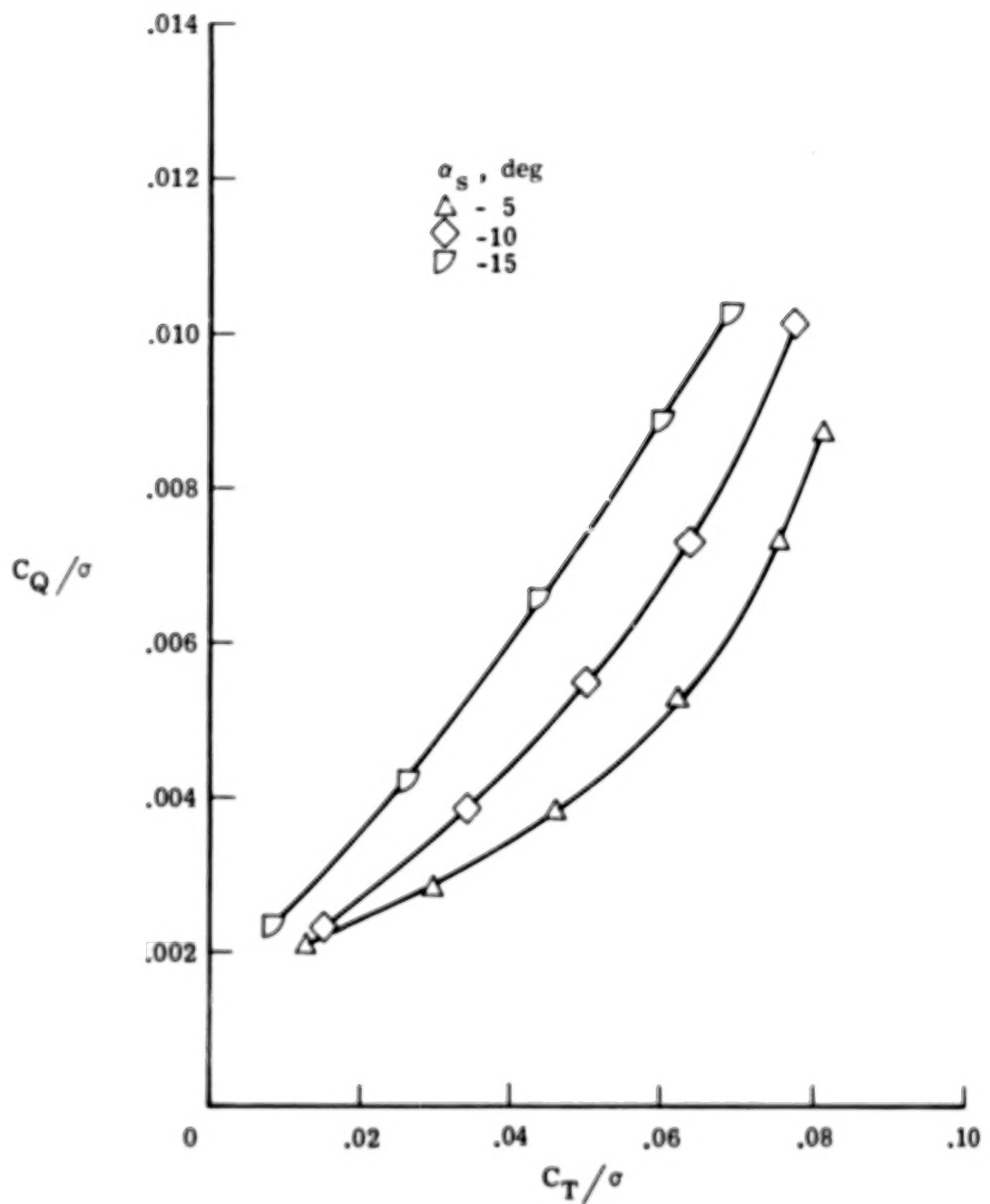
(a) $\mu = 0.22$.

Figure 12.- Variation of rotor torque with thrust for forward flight. $\Delta B_1 = 0^{\circ}$.



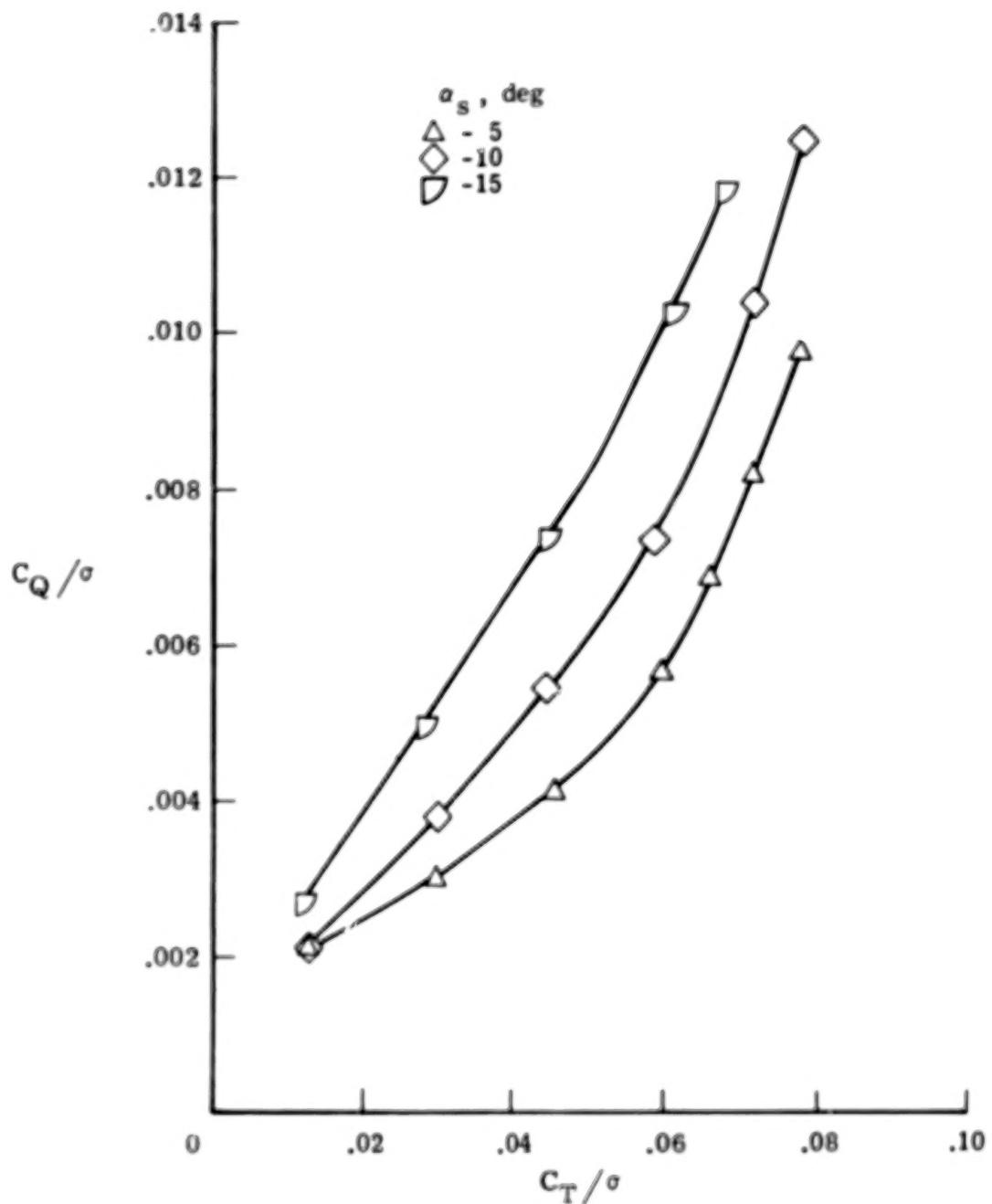
(b) $\mu = 0.30.$

Figure 12.- Continued.



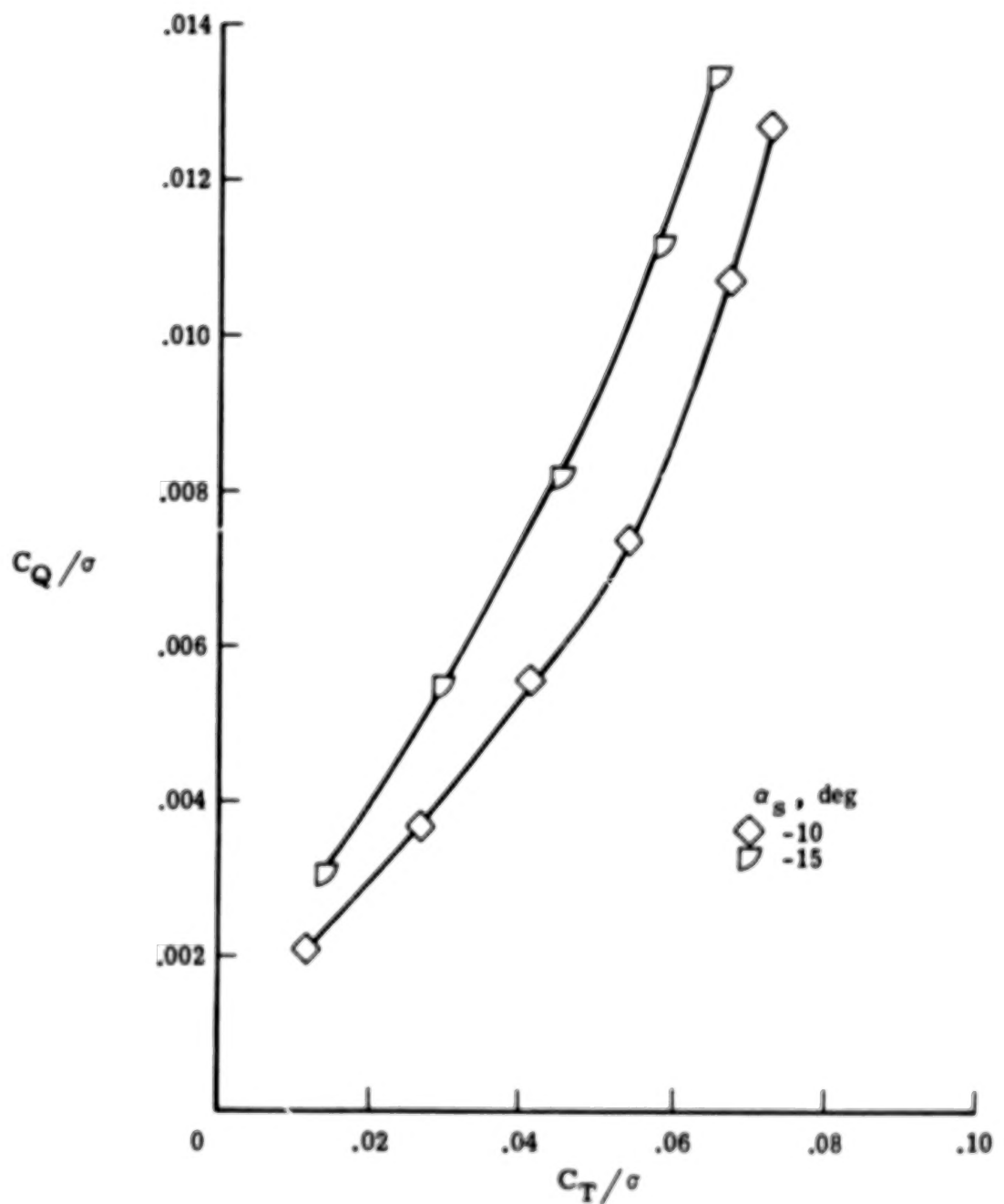
(c) $\mu = 0.35.$

Figure 12.- Continued.



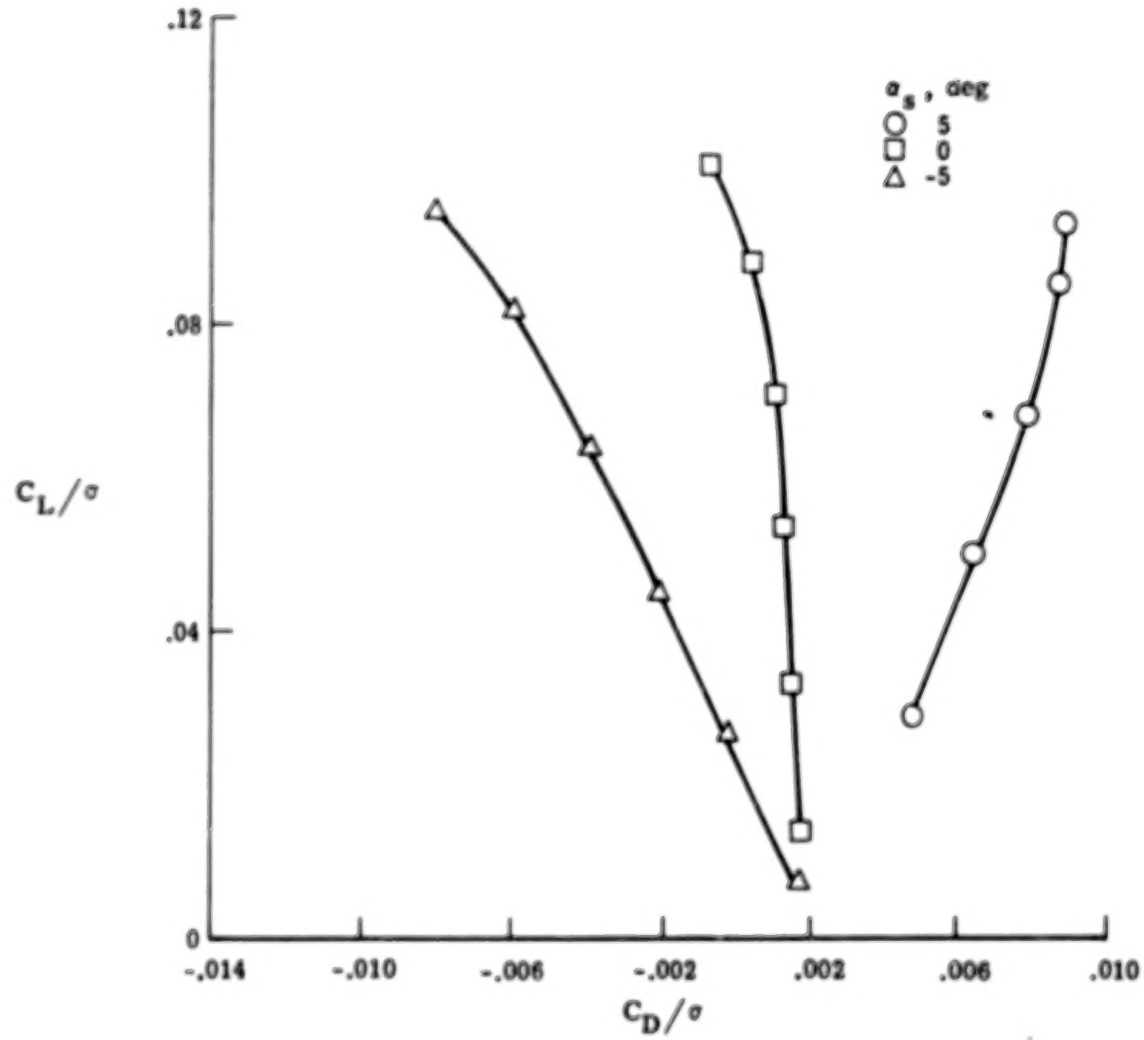
(d) $\mu = 0.40.$

Figure 12.- Continued.



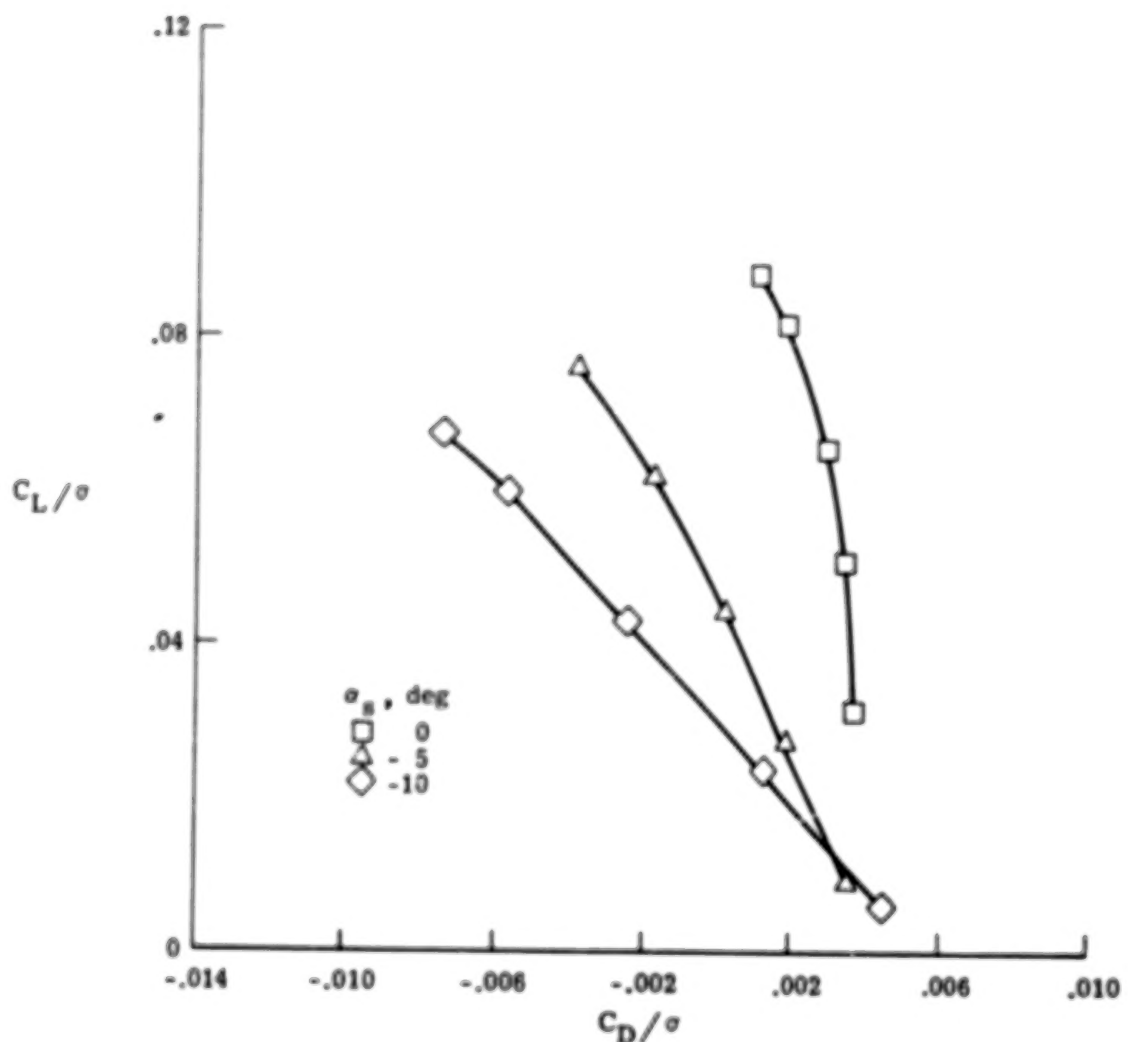
(e) $\mu = 0.45.$

Figure 12. - Concluded.



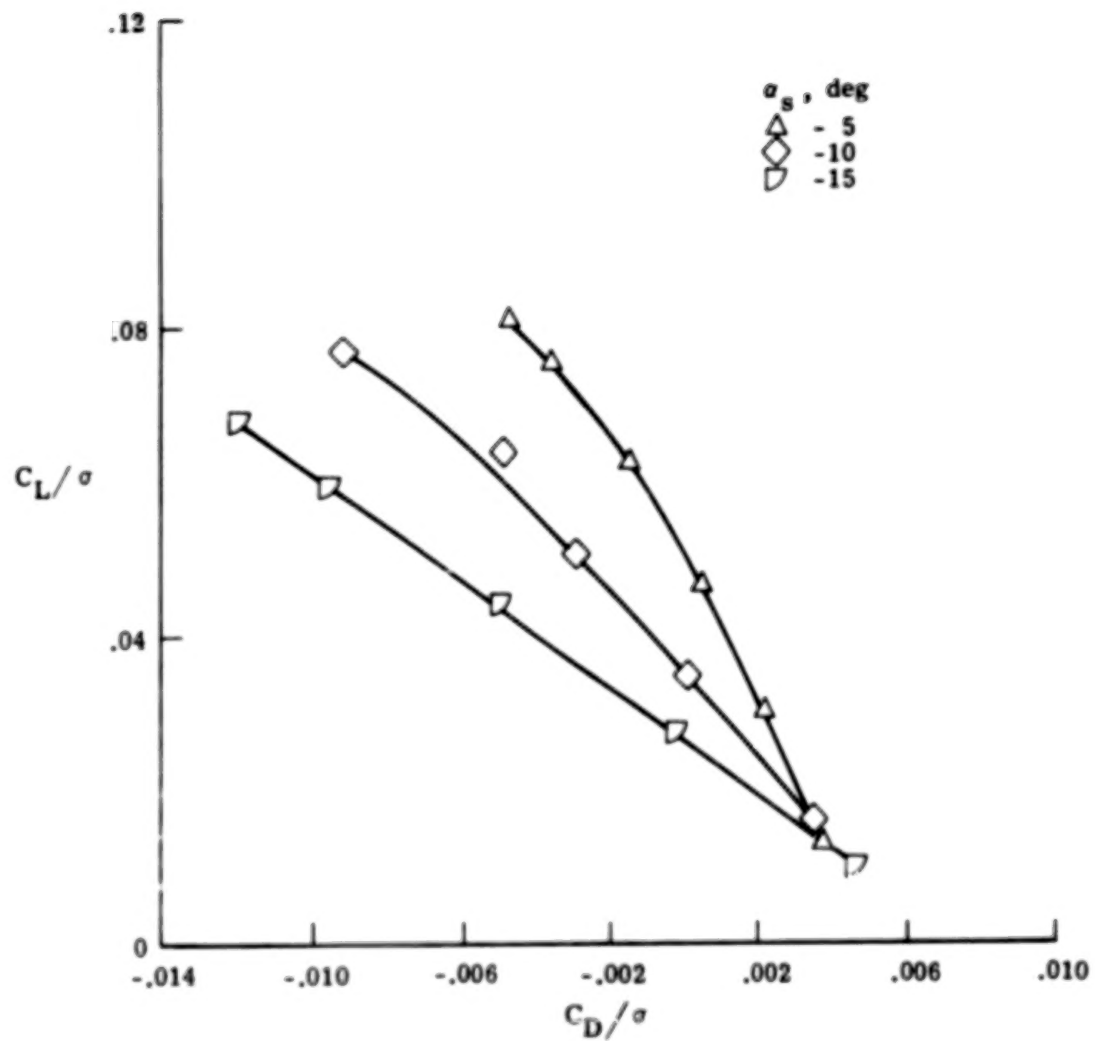
(a) $\mu = 0.22$.

Figure 13.- Variation of rotor lift with drag for forward flight. $\Delta B_1 = 0^\circ$.



(b) $\mu = 0.30.$

Figure 13.- Continued.



(c) $\mu = 0.35.$

Figure 13.- Continued.

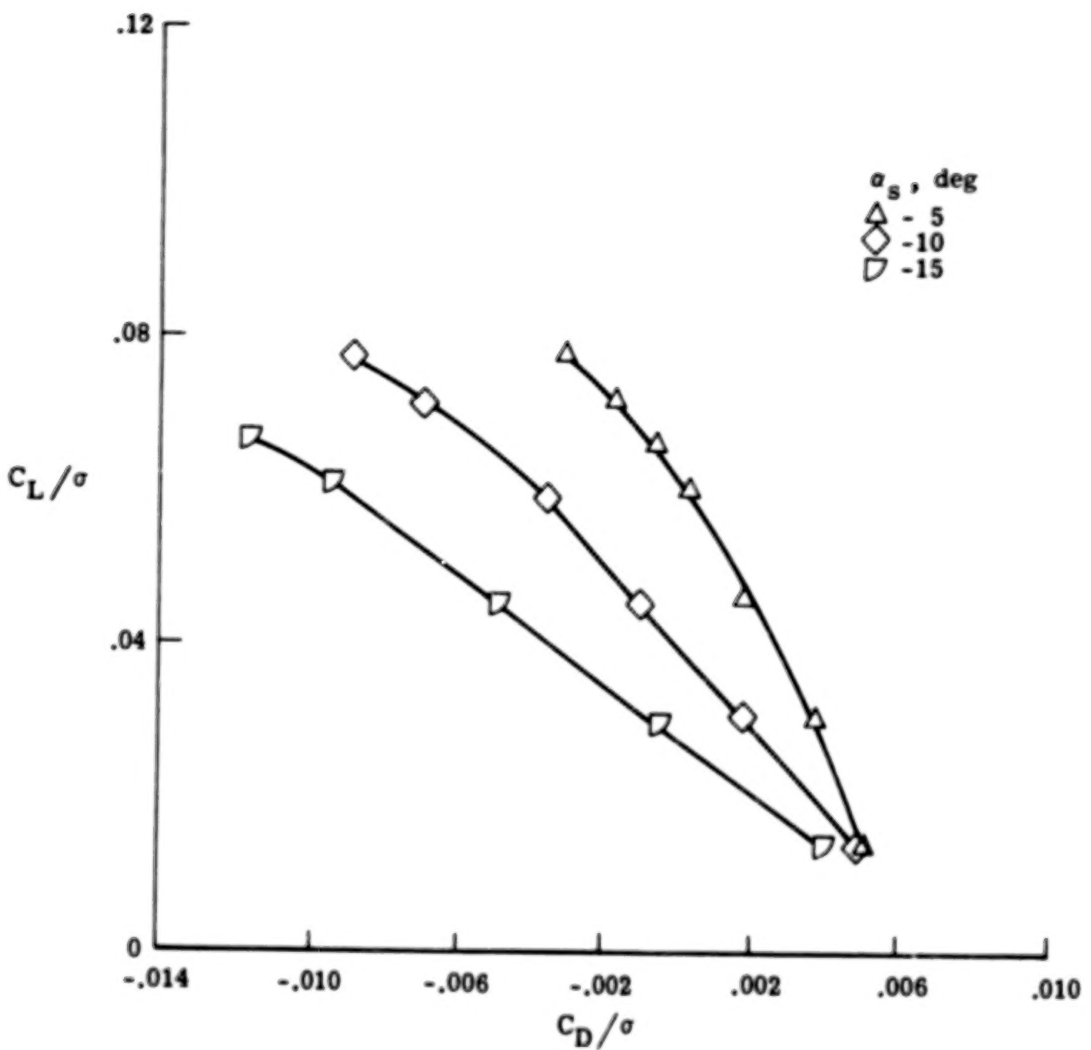
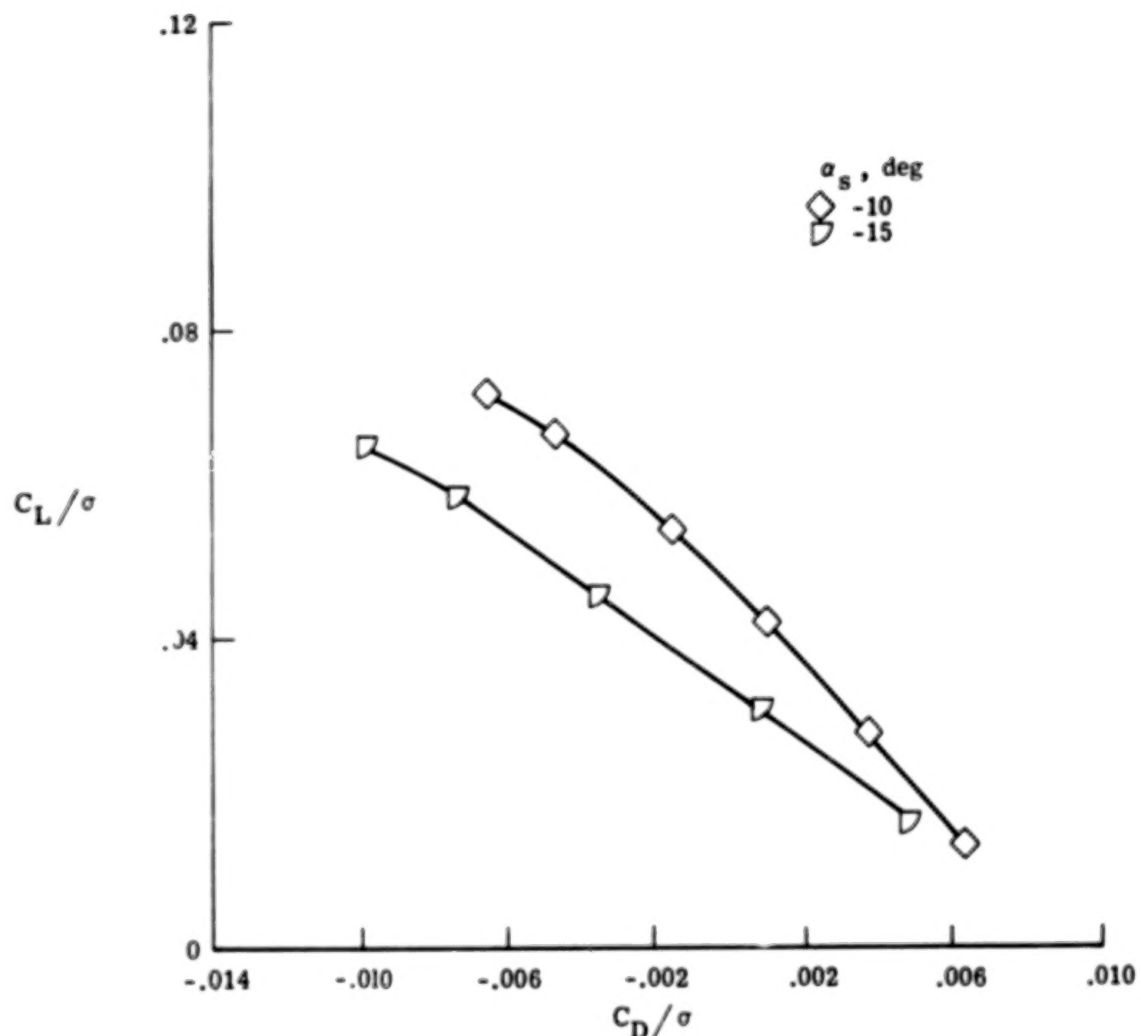
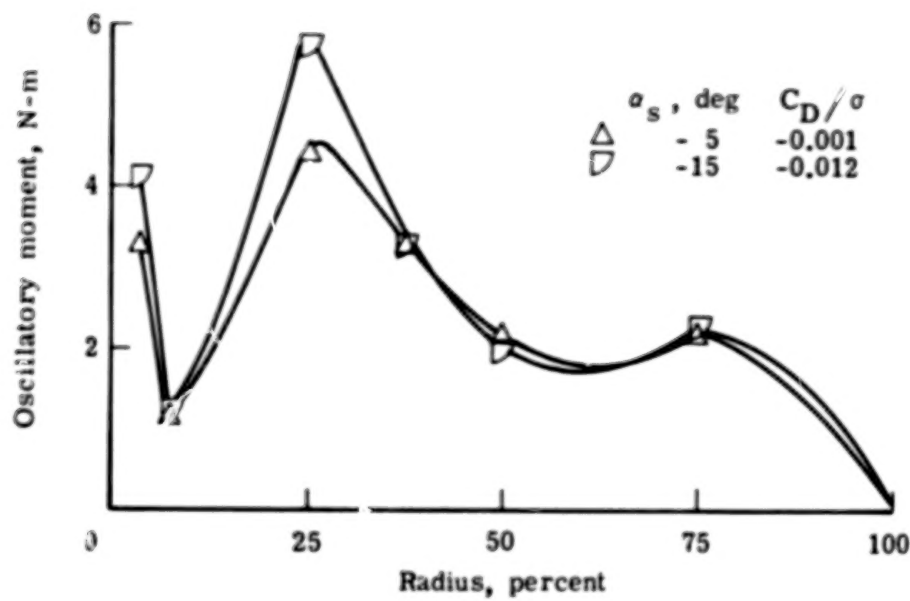


Figure 13.- Continued.

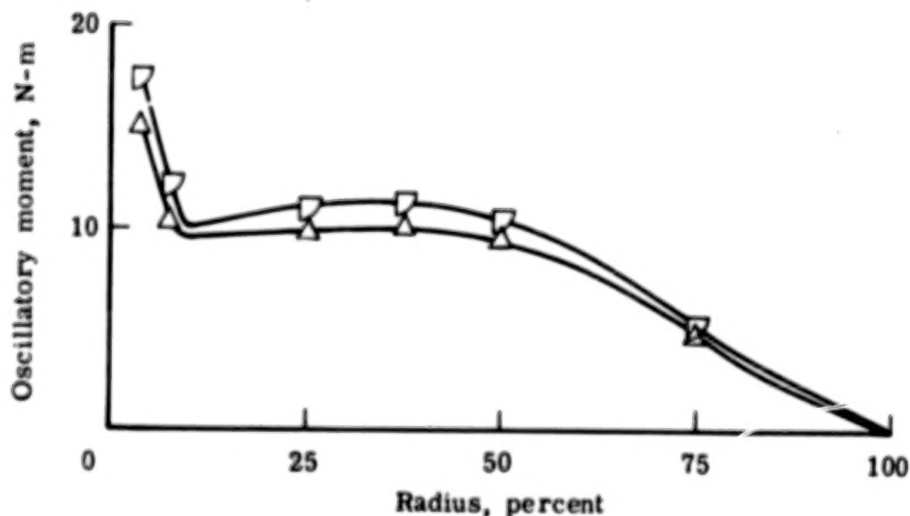


(e) $\mu = 0.45$.

Figure 13.- Concluded.

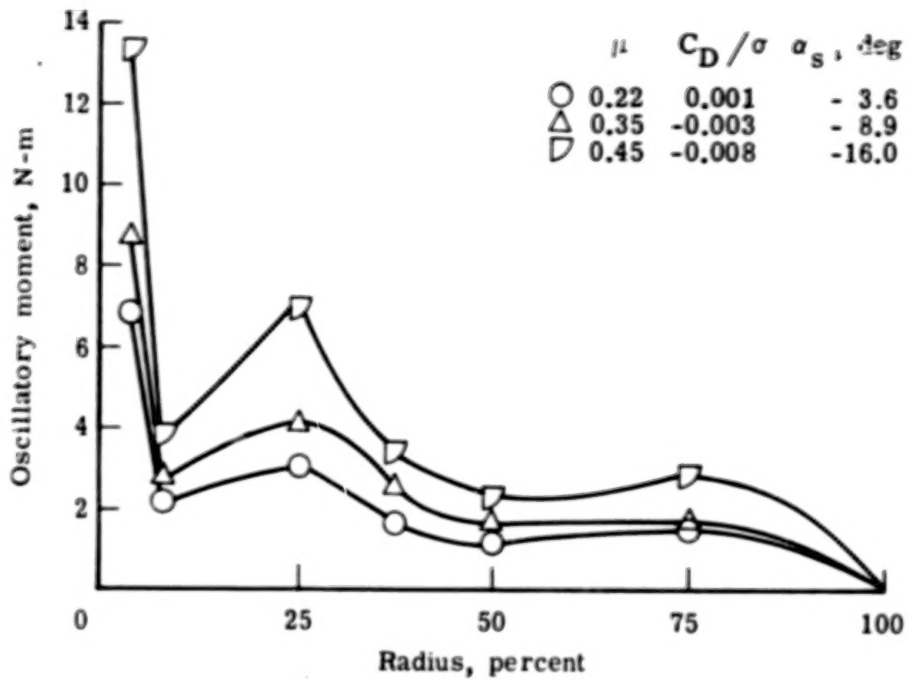


(a) Beam bending.

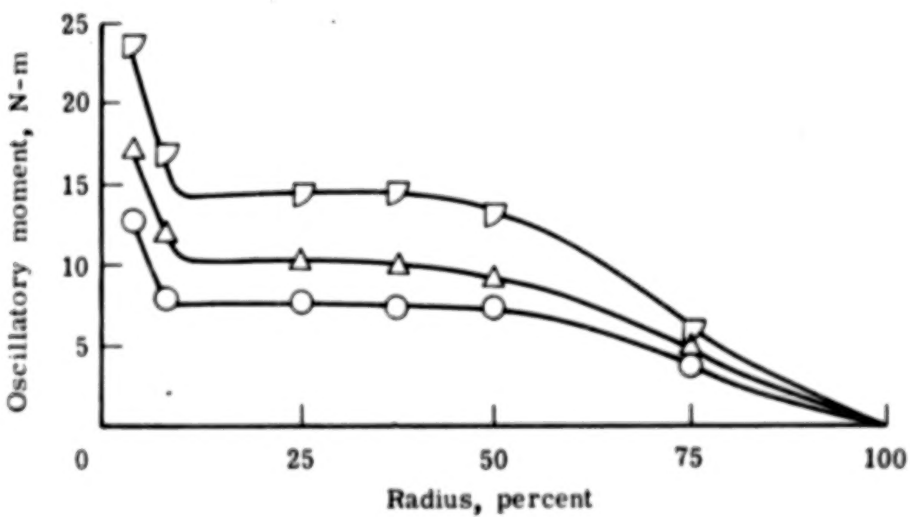


(b) Chord bending.

Figure 14. - Spanwise oscillatory moment distributions for two shaft angles. $\mu = 0.4$; $C_L/\sigma = 0.066$; $\Delta B_1 = 0^\circ$.

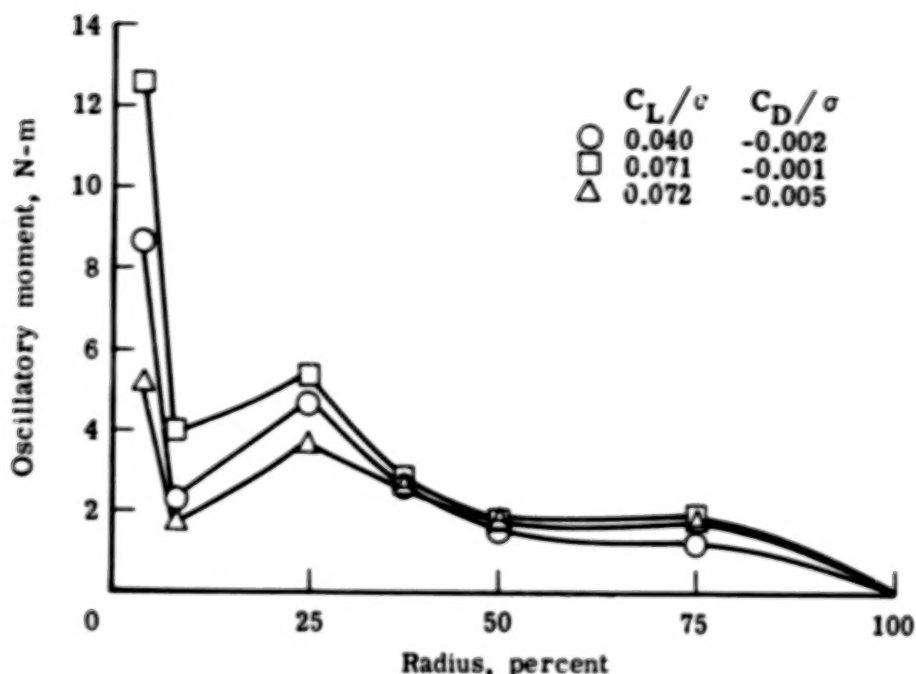


(a) Beam bending.

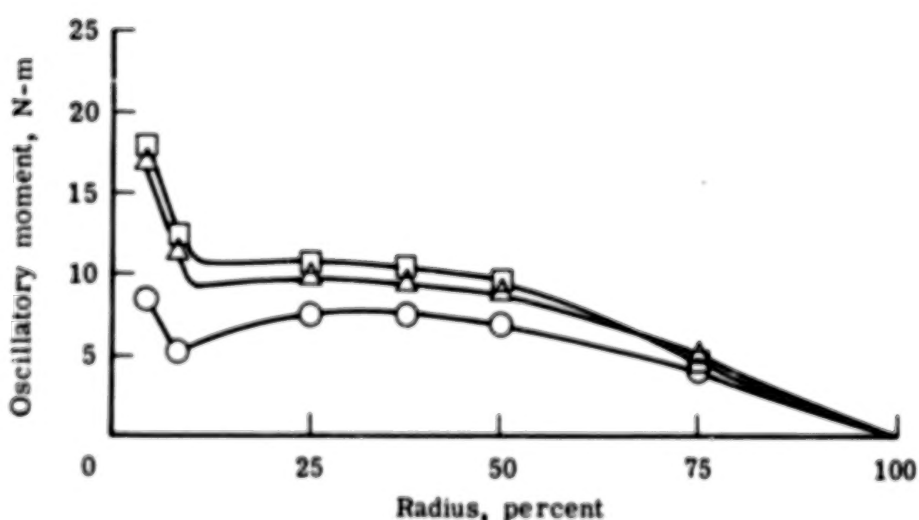


(b) Chord bending.

Figure 15. - Spanwise oscillatory moment distributions for three advance ratios. $C_L/\sigma = 0.07$; $\Delta B_1 \neq 0^\circ$.

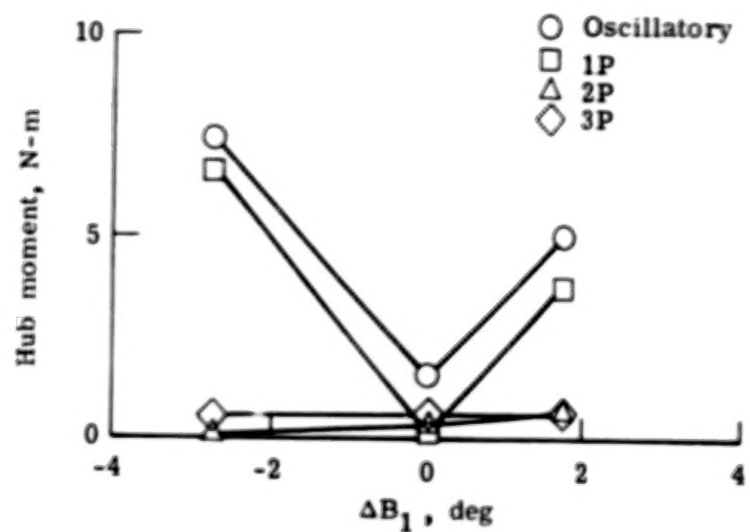


(a) Beam bending.

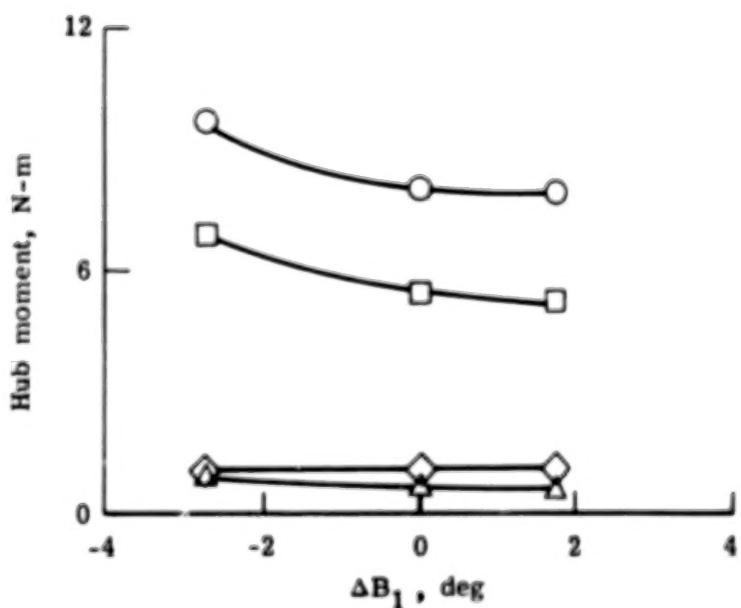


(b) Chord bending.

Figure 16.- Spanwise oscillatory moment distributions for three values of lift and drag. $\mu = 0.35$; $\alpha_g = -8.9^\circ$; $\Delta B_1 \neq 0^\circ$.

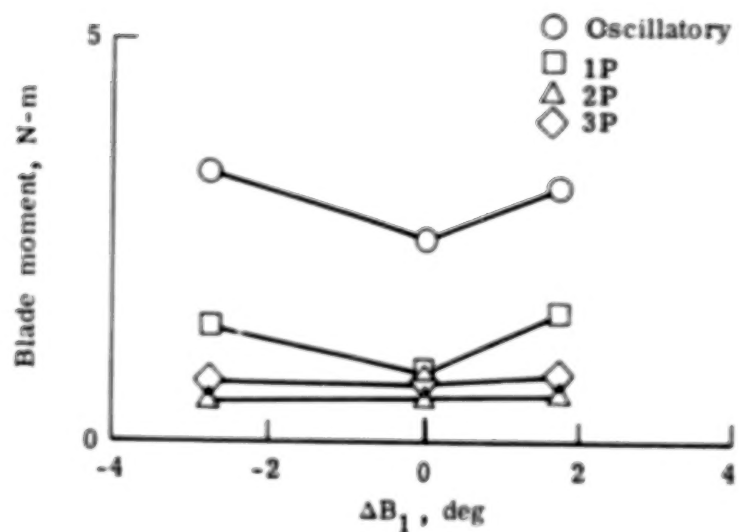


(a) Beam bending.

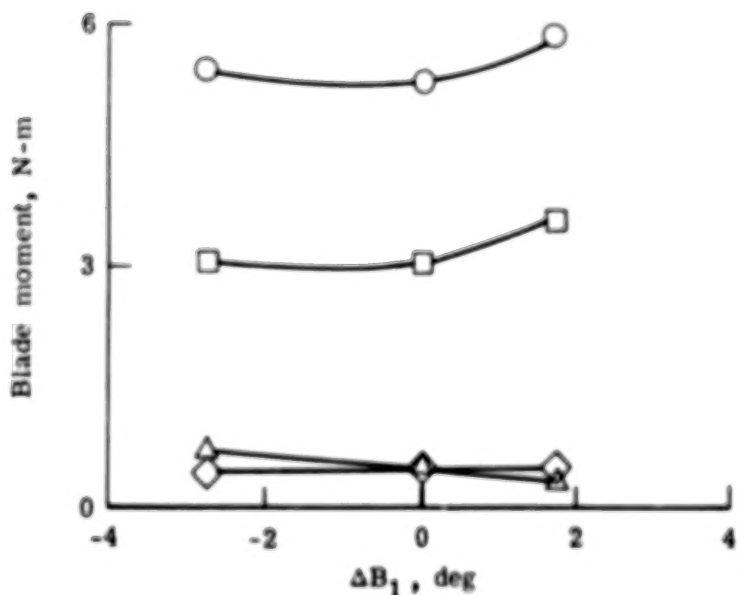


(b) Chord bending.

Figure 17.- Variation of hub ($x = 0.04$) moments with changes in longitudinal cyclic pitch. $\mu = 0.3$; $\alpha_s = -6.6^\circ$; $C_L/\sigma = 0.06$.

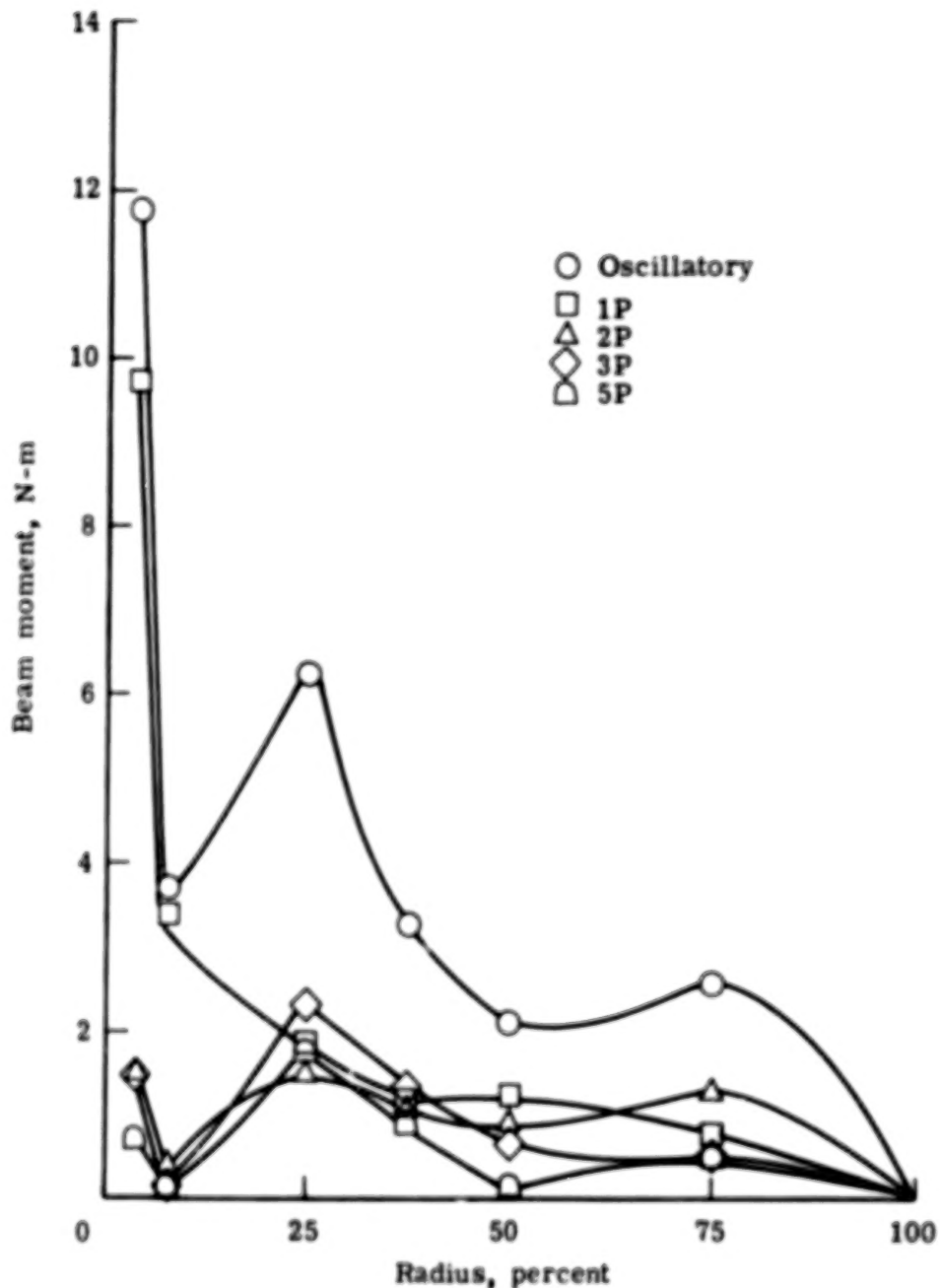


(a) Beam bending.



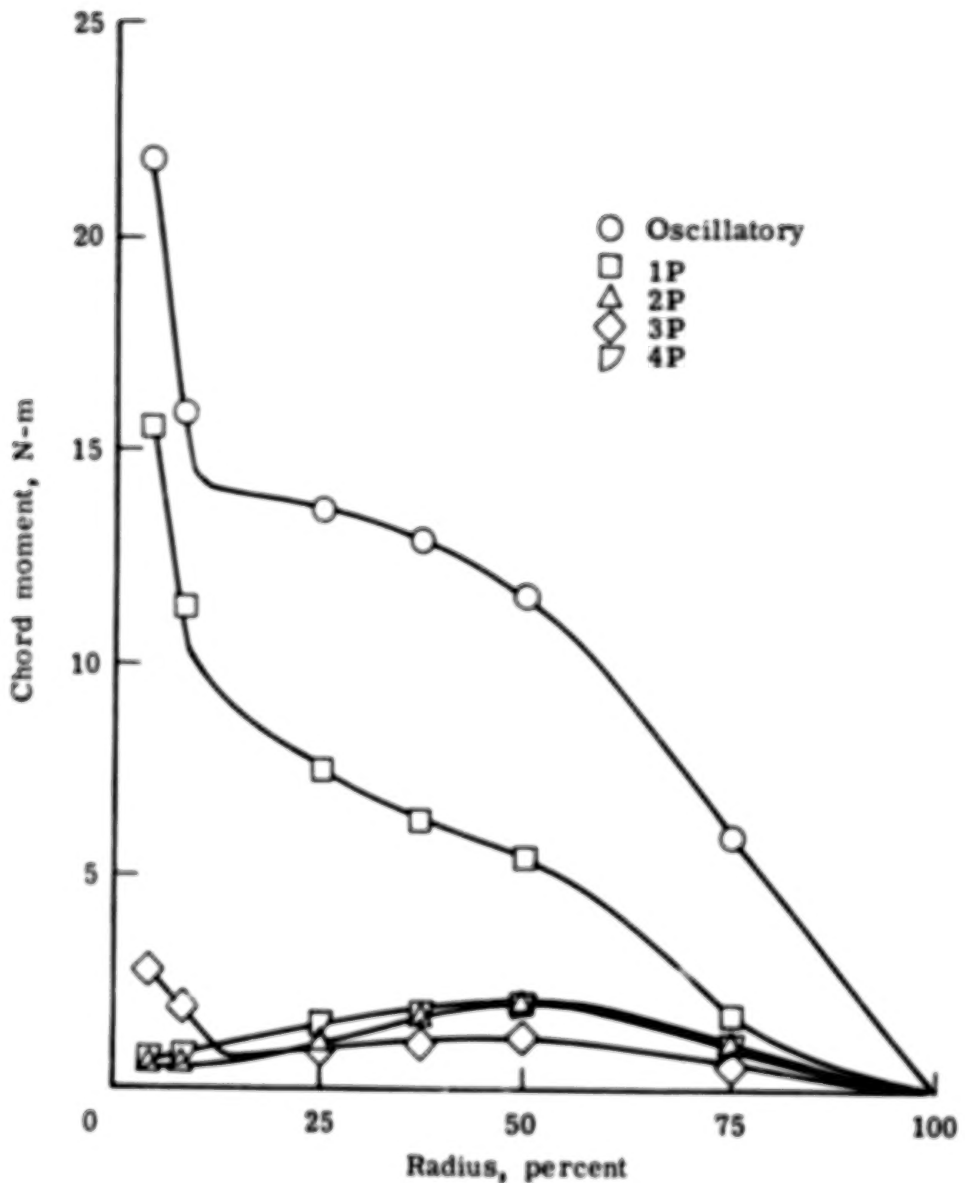
(b) Chord bending.

Figure 18.- Variation of blade ($x = 0.25$) moments with changes in longitudinal cyclic pitch.
 $\mu = 0.3$; $\alpha_s = -6.6^\circ$; $C_L/\sigma = 0.06$.



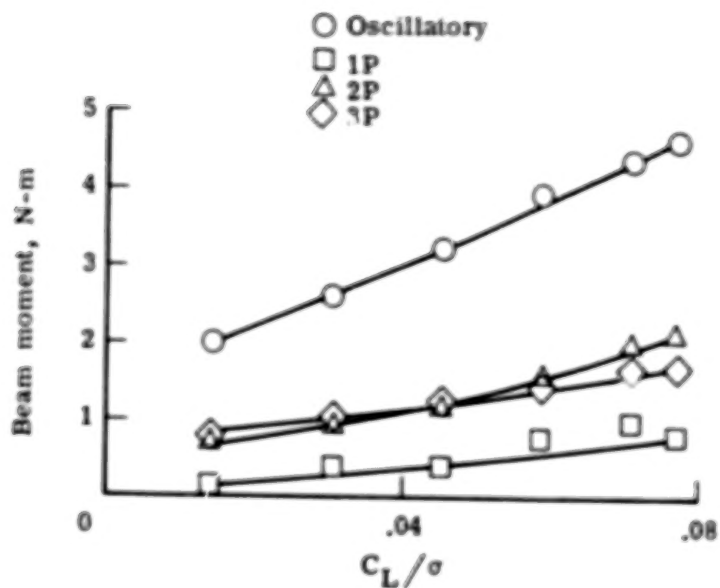
(a) Beam bending.

Figure 19.- Spanwise oscillatory and harmonic moment distributions. $\mu = 0.4$; $\alpha_s = -12.5^\circ$; $C_L/\sigma = 0.074$; $C_D/\sigma = -0.006$; $\Delta B_1 \neq 0^\circ$.

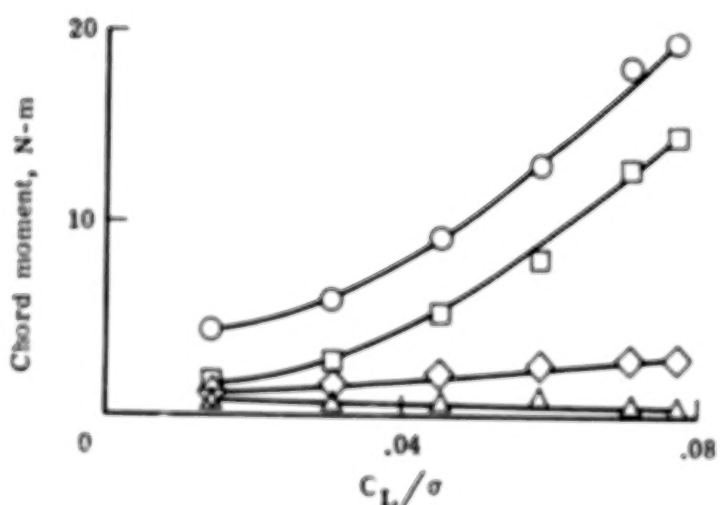


(b) Chord bending.

Figure 19.- Concluded.

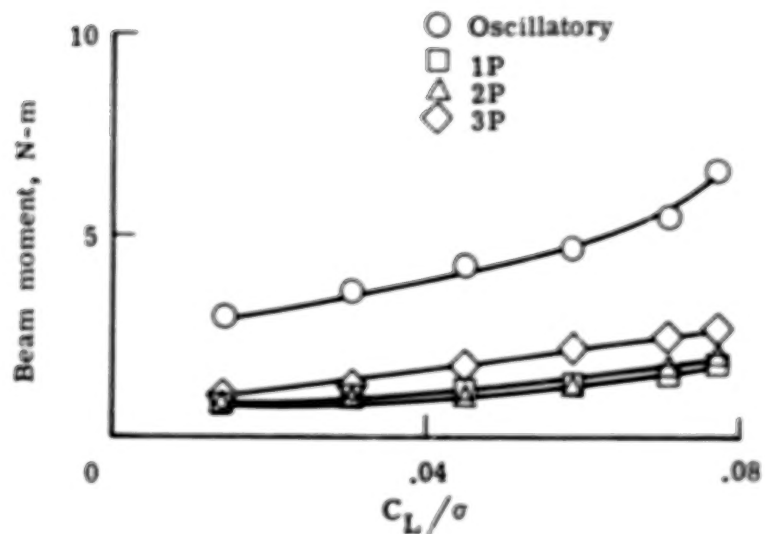


(a) Beam bending at $x = 0.04$.

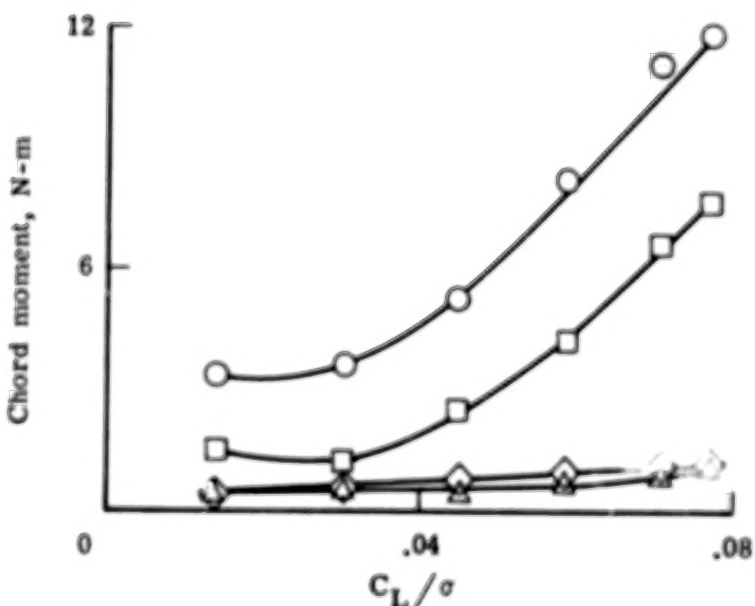


(b) Chord bending at $x = 0.04$.

Figure 20.- Variation of rotor response with lift. $\mu = 0.40$; $\sigma_s = -10^\circ$; $\Delta B_1 = 0^\circ$.

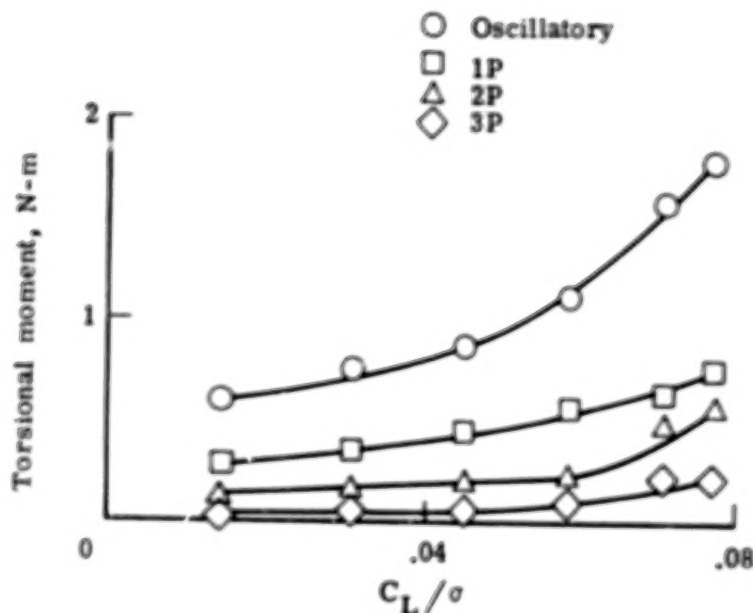


(c) Beam bending at $x = 0.25$.

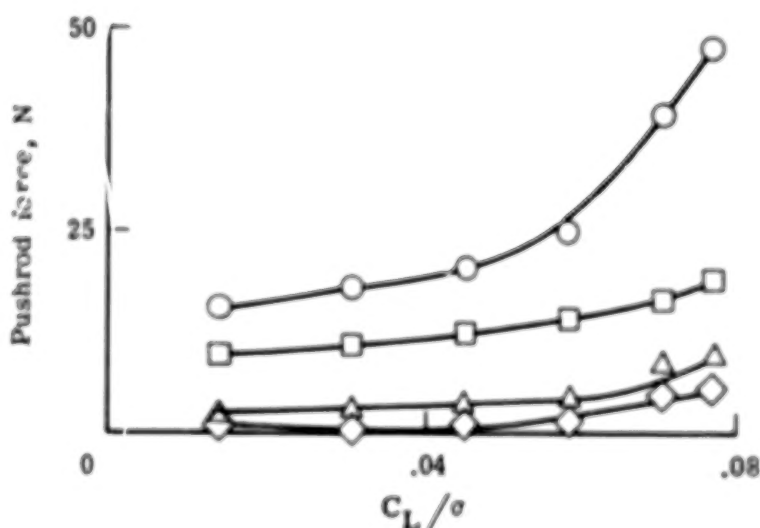


(d) Chord bending at $x = 0.25$.

Figure 20.- Continued.

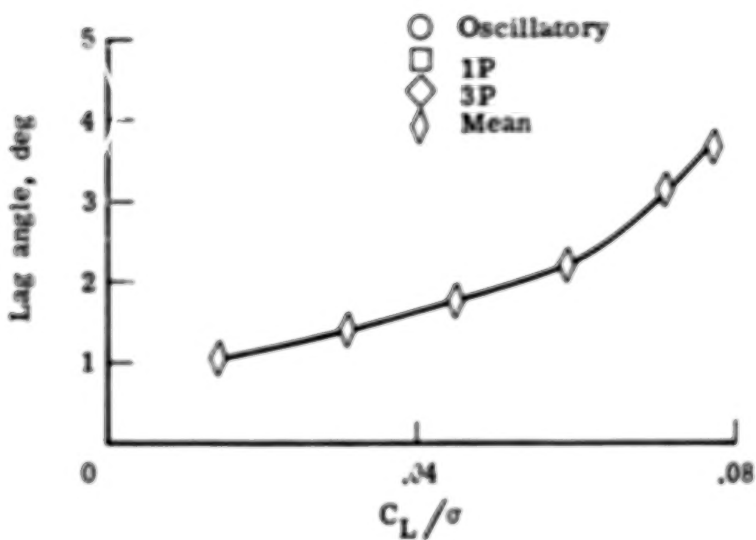


(e) Torsional moment at $x = 0.50$.

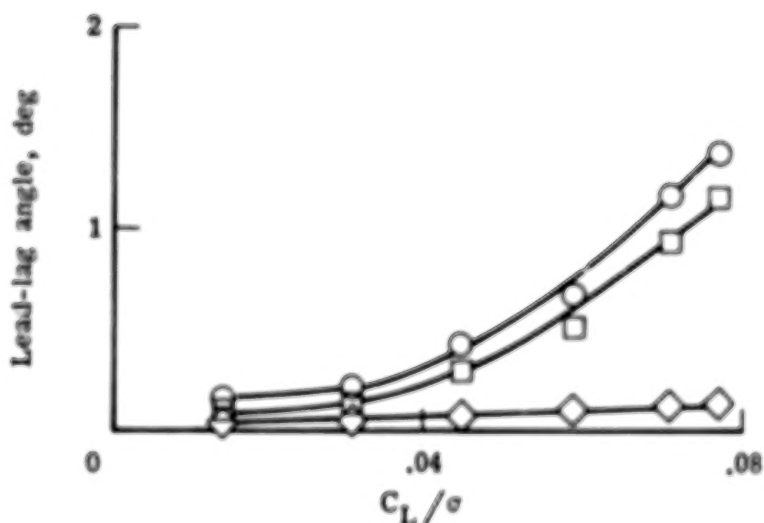


(f) Pushrod axial force.

Figure 20.- Continued.



(g) Blade mean lag angle about hinge.



(h) Blade lead-lag motion about hinge.

Figure 20.- Concluded.

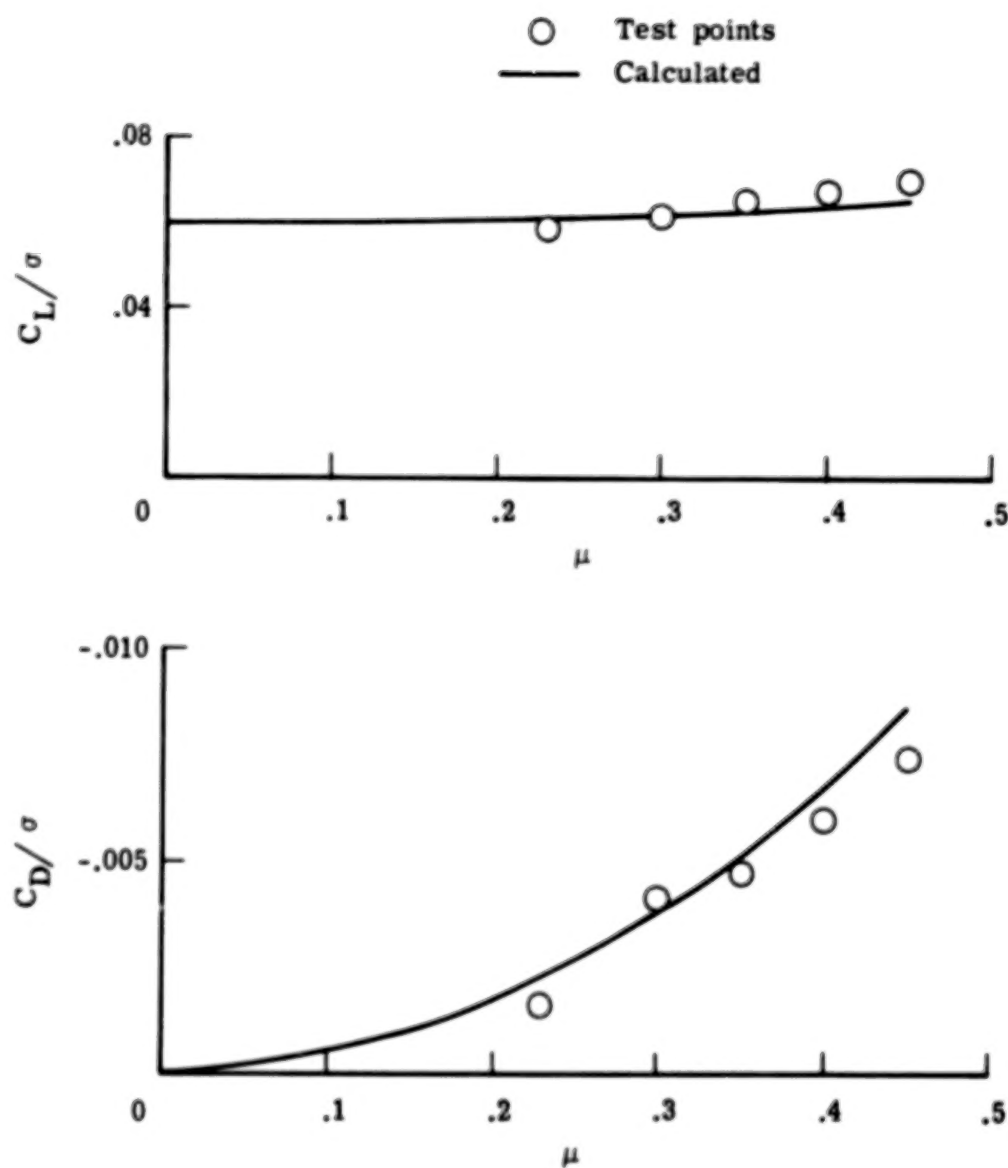
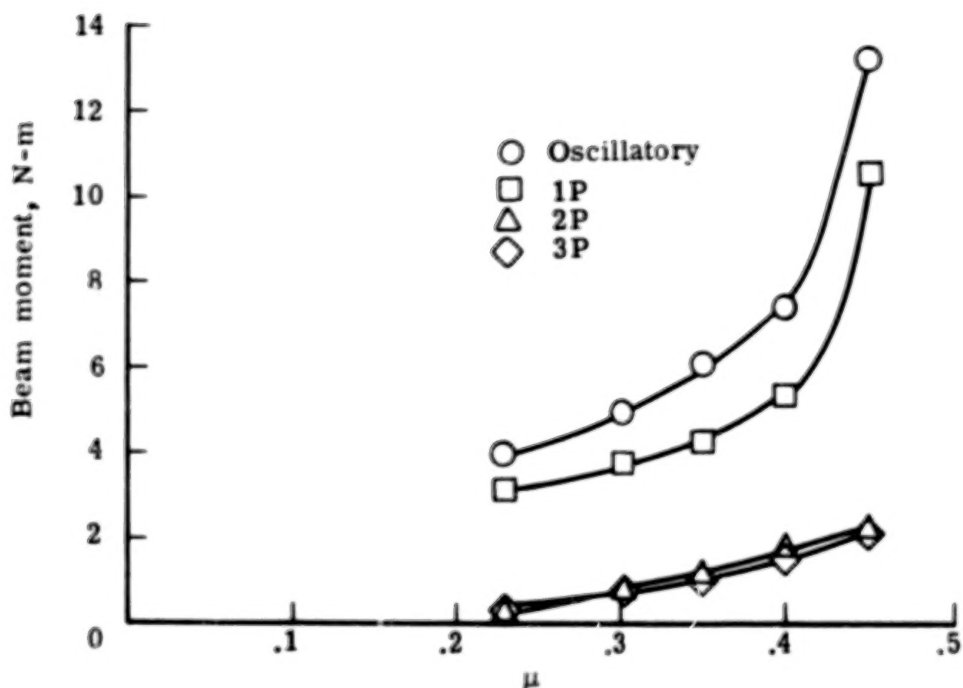
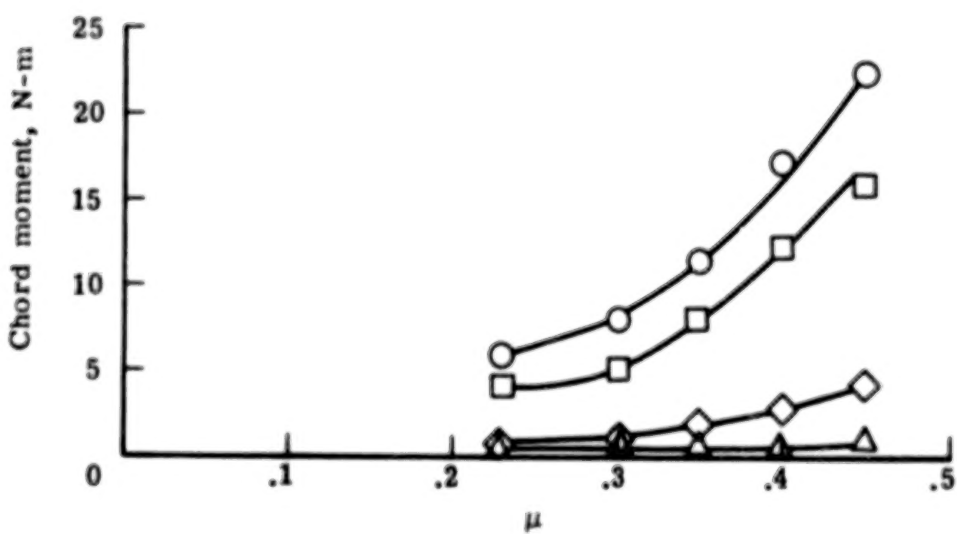


Figure 21.- Rotor lift and drag requirements in forward flight.
 $\Delta B_1 \neq 0^\circ$.

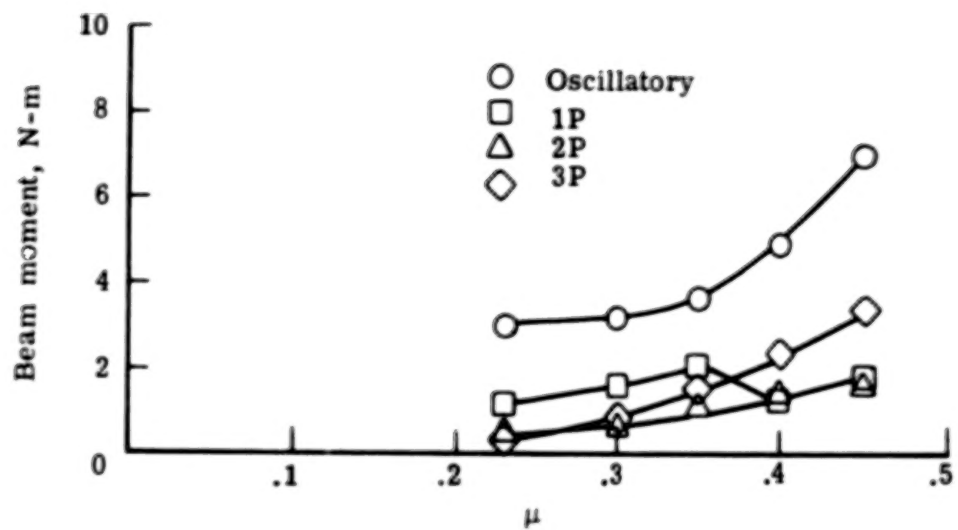


(a) Beam bending at $x = 0.04$.

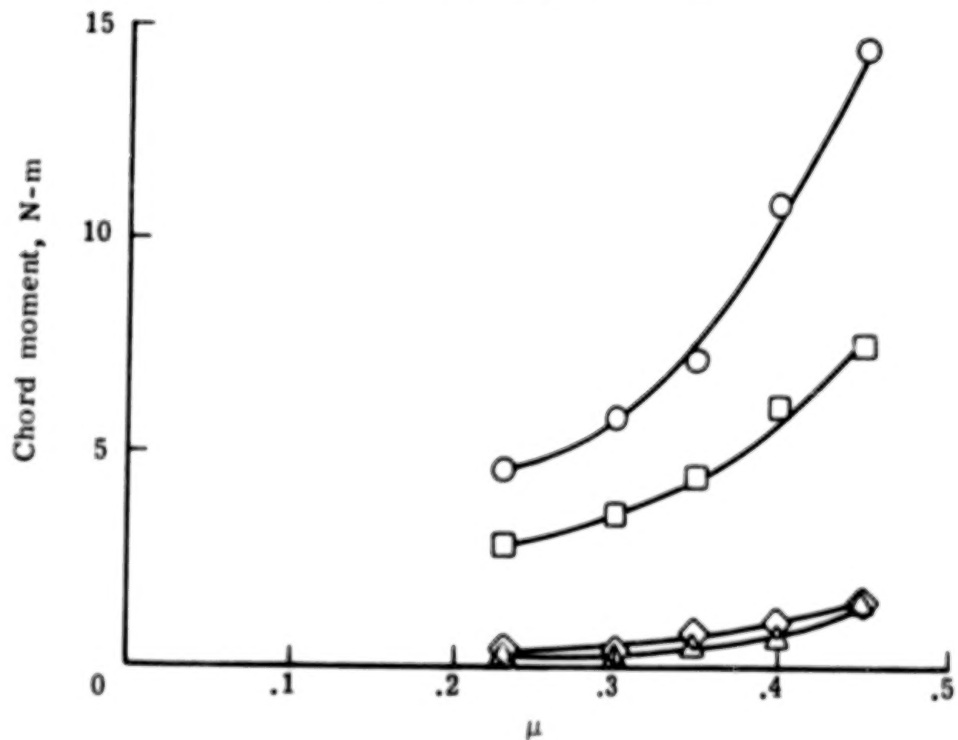


(b) Chord bending at $x = 0.04$.

Figure 22.- Variation of rotor response with advance ratio.
 $\Delta B_1 \neq 0^\circ$.

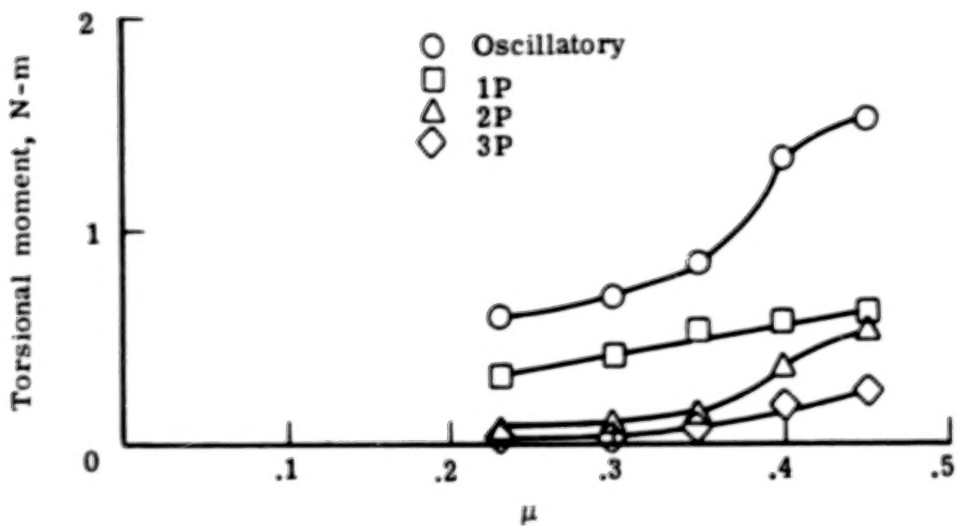


(c) Beam bending at $x = 0.25$.

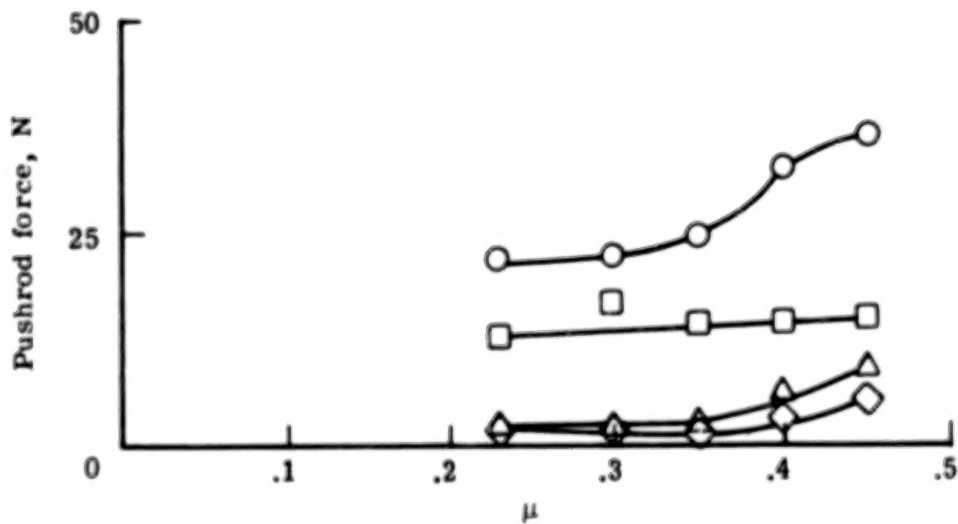


(d) Chord bending at $x = 0.25$.

Figure 22.- Continued.

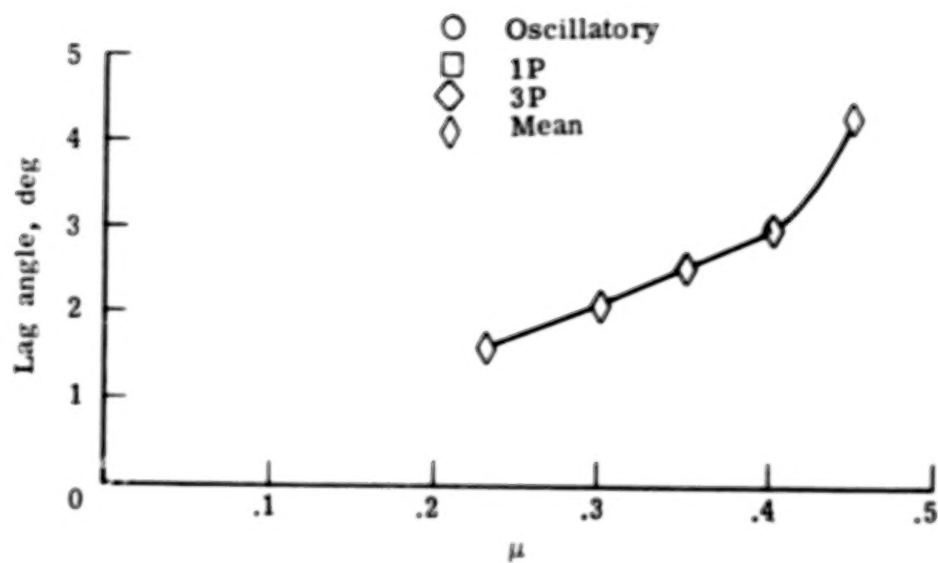


(e) Torsional moment at $x = 0.50$.

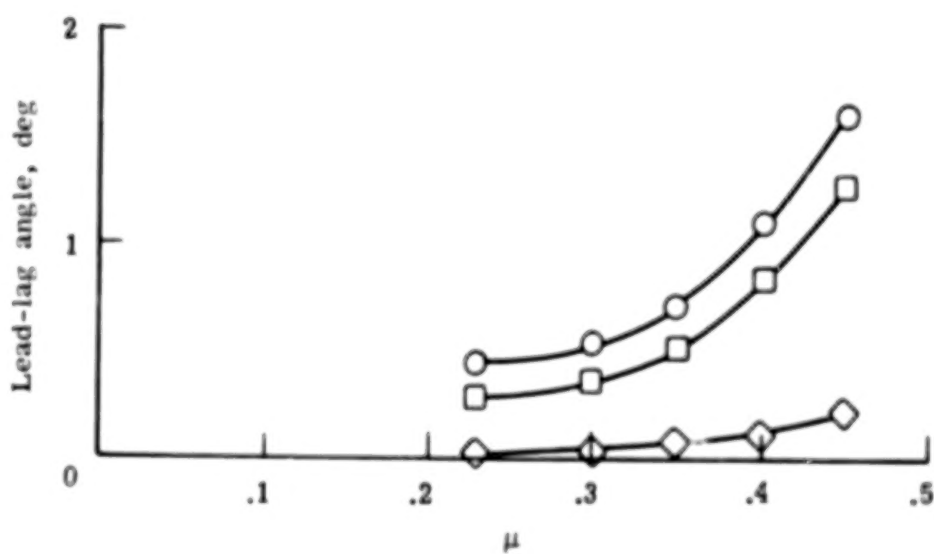


(f) Pushrod axial force.

Figure 22.- Continued.



(g) Blade mean lag angle about hinge.



(h) Blade lead-lag motion about hinge.

Figure 22. - Concluded.

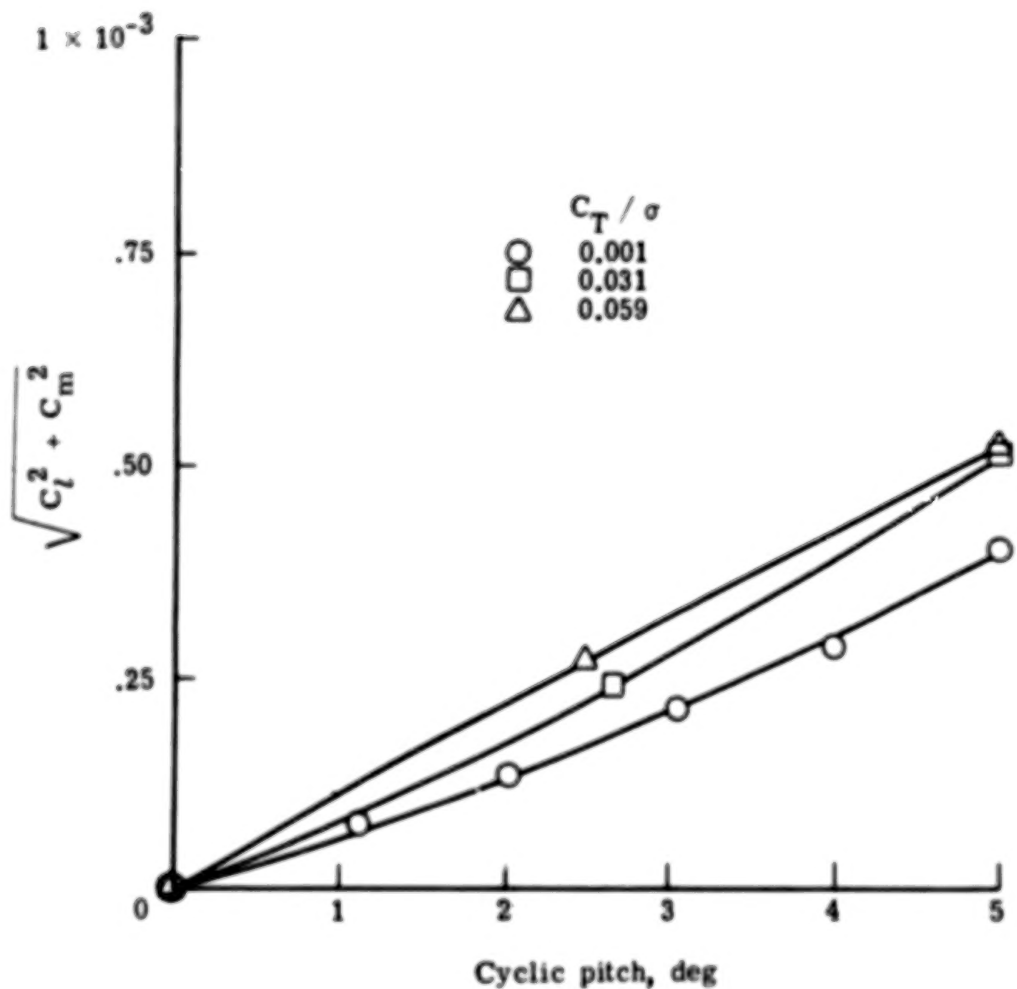


Figure 23.- Rotor hub moment coefficient resulting from application of cyclic pitch during hover.

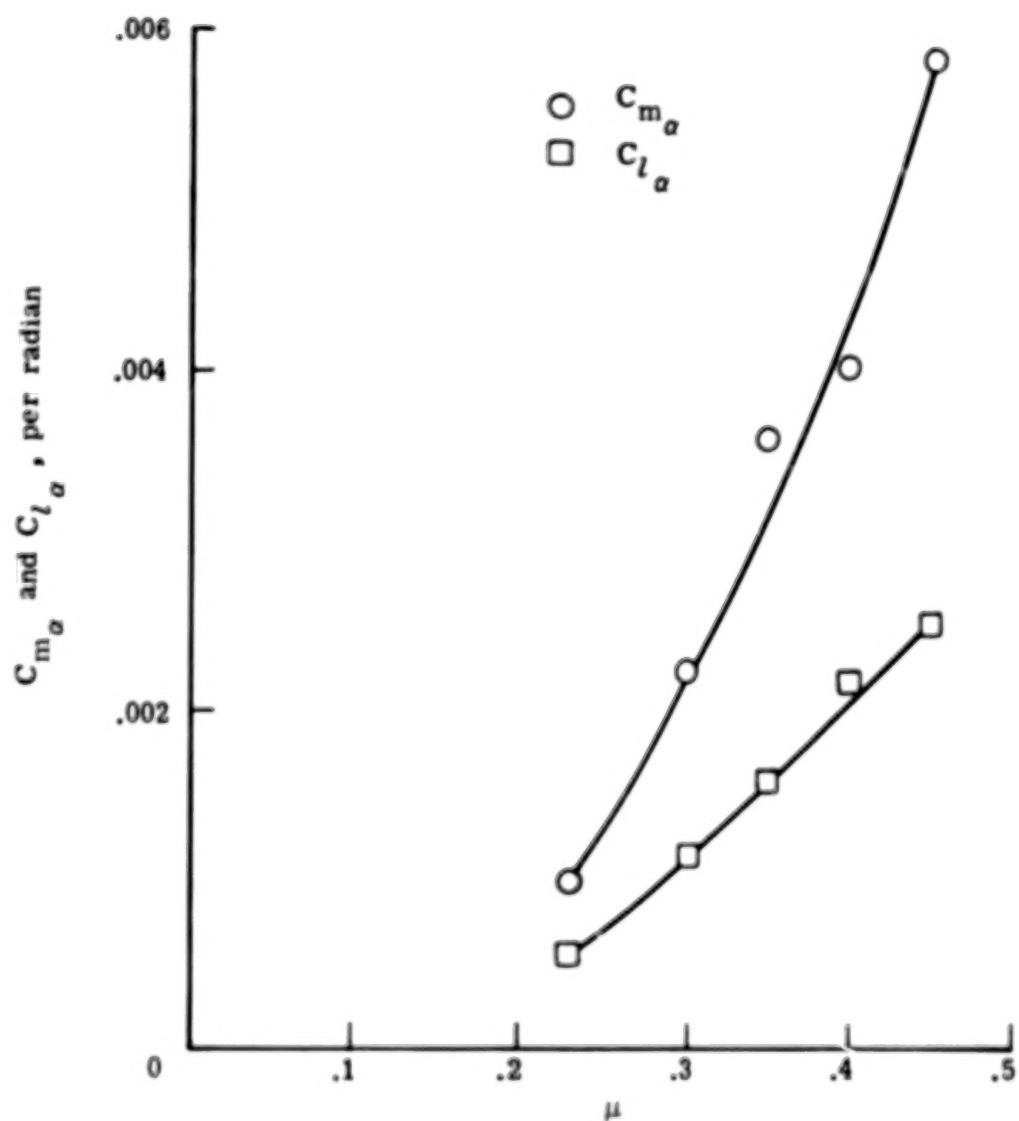


Figure 24.- Variations of the shaft-angle derivatives of the hub moment coefficients with advance ratio.

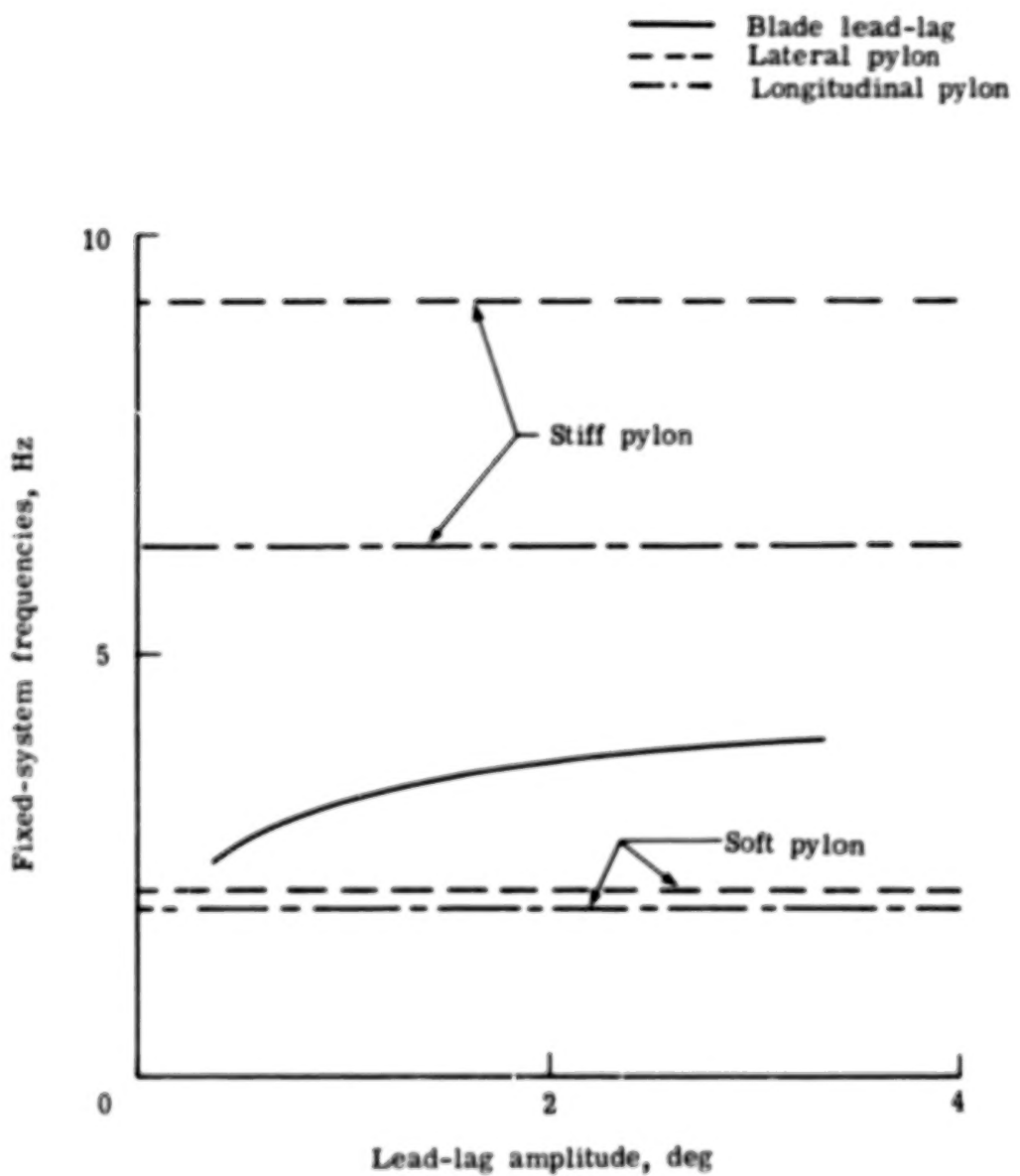


Figure 25.- Uncoupled blade and pylon resonance frequencies.
 $\Omega = 64.4 \text{ rad/s.}$

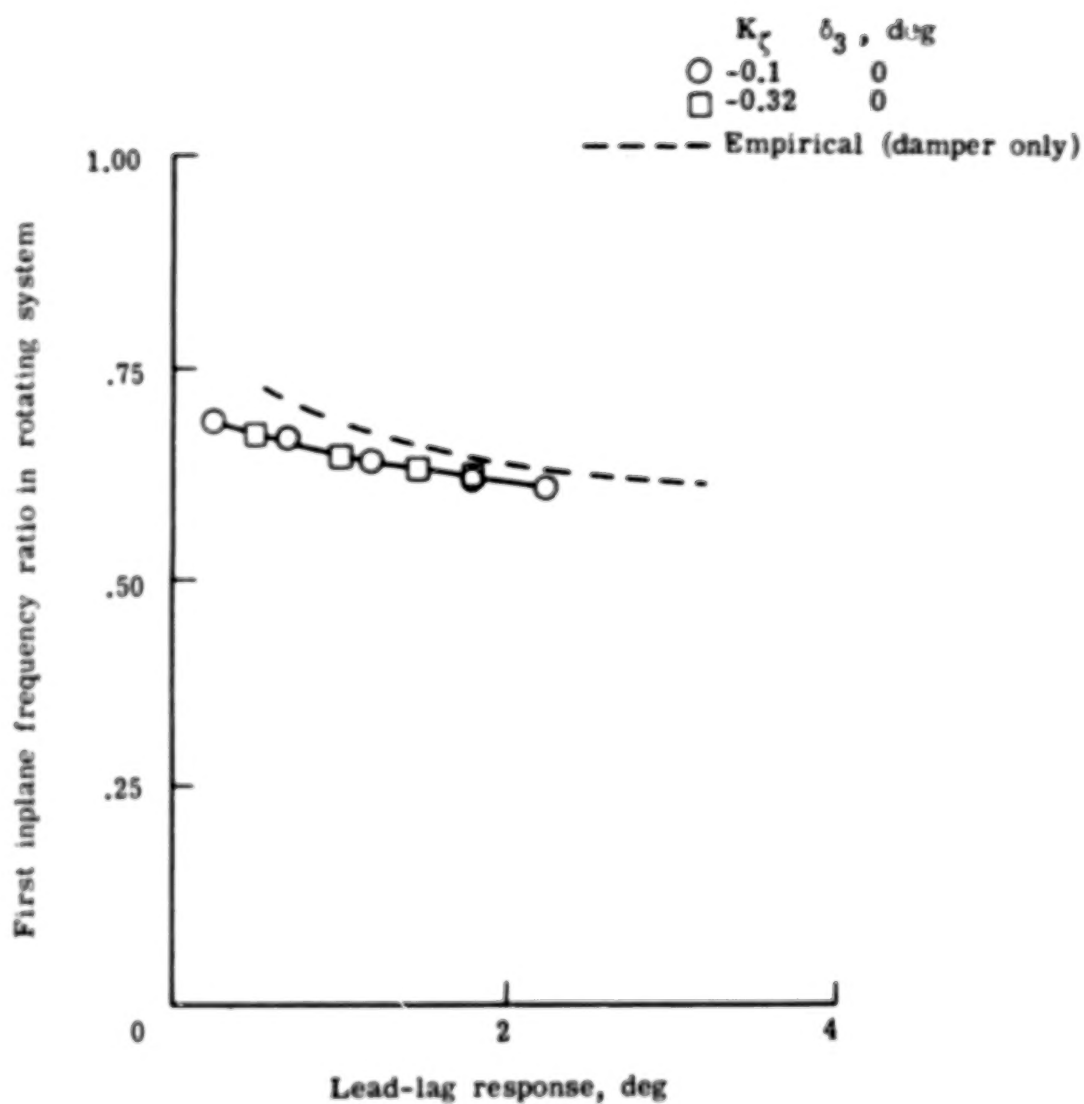


Figure 26.- Lead-lag frequency for stiff-pylon mounting in hover.
 $\Omega = 64.4$ rad/s; $0 \leq C_T/\sigma \leq 0.06$.

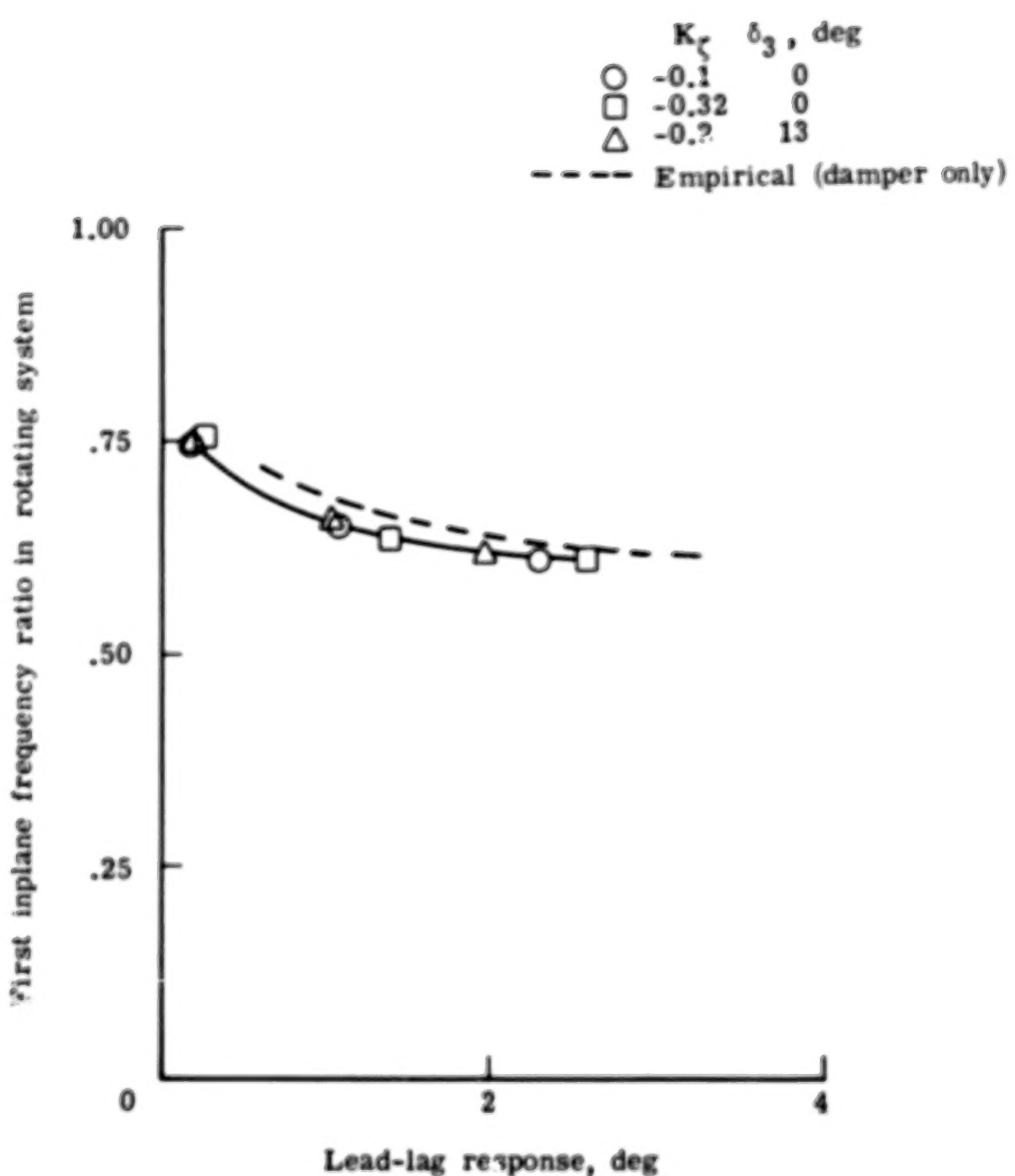


Figure 27. - Lead-lag frequency for soft-pylon mounting in hover.
 $\Omega = 64.4$ rad/s; $0 \leq C_T/\sigma \leq 0.06$.

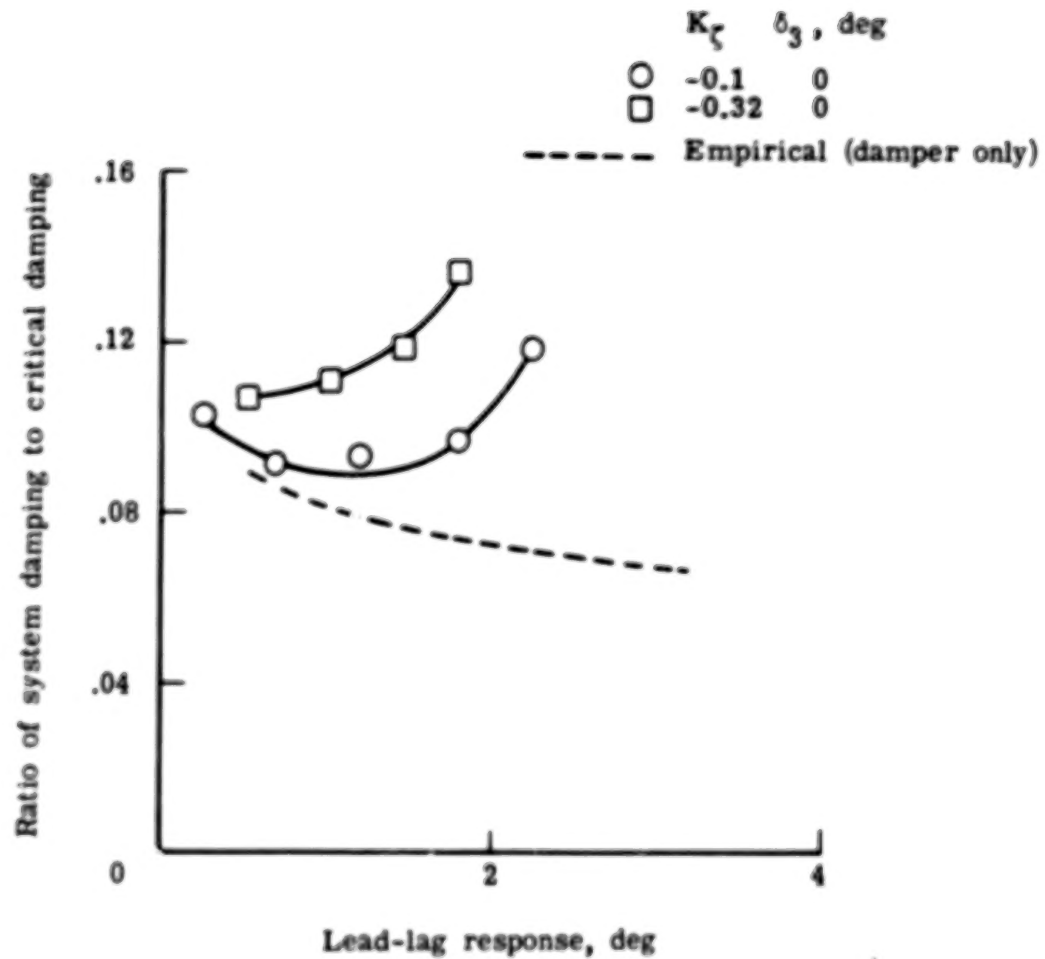


Figure 28.- Lead-lag damping for stiff-pylon mounting in hover.

$\Omega = 64.4$ rad/s; $0 \leq C_T/\sigma \leq 0.06$.

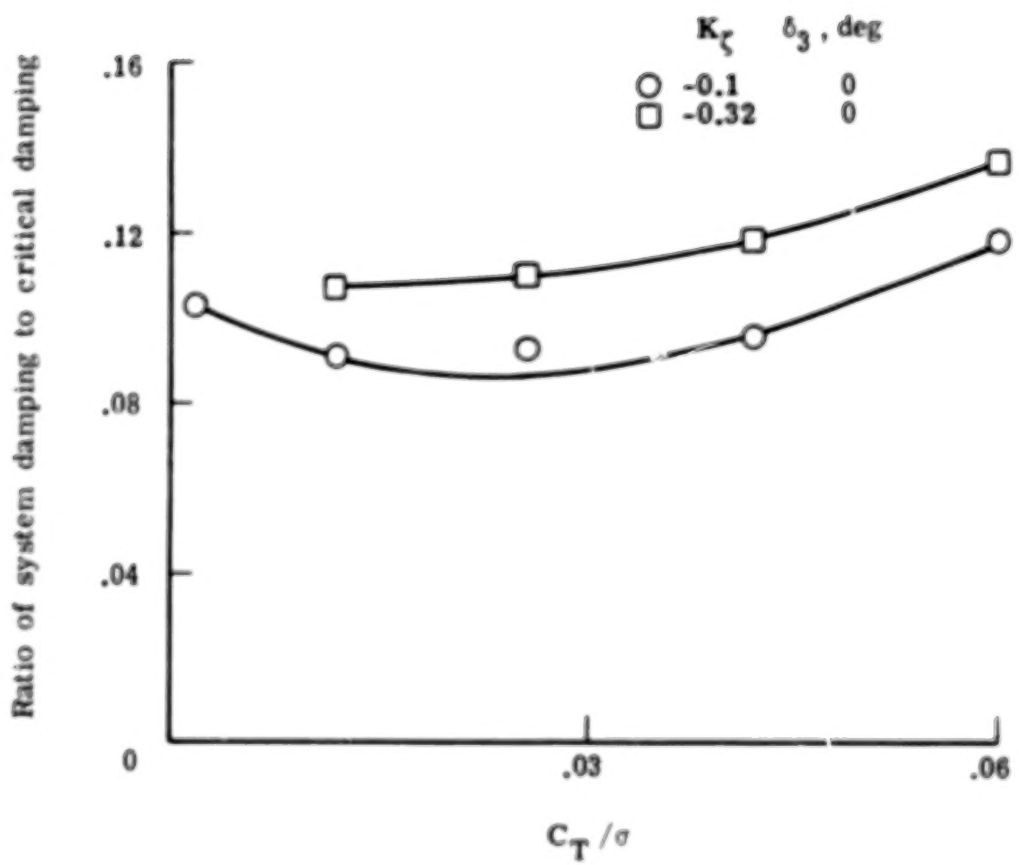


Figure 29.- Variation of lead-lag damping with thrust for stiff-pylon mounting in hover. $\Omega = 64.4$ rad/s.

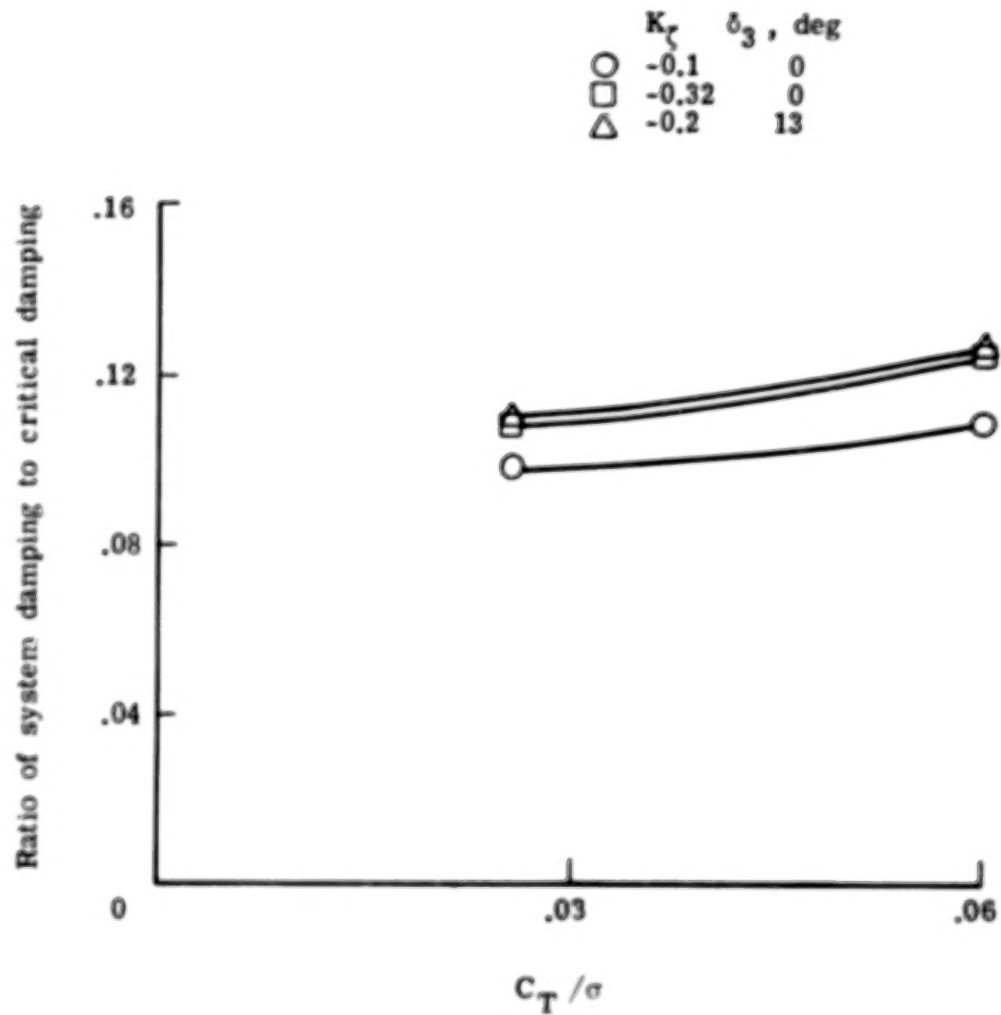


Figure 30.- Variation of lead-lag damping with thrust for soft-pylon mounting in hover. $\Omega = 64.4$ rad/s.

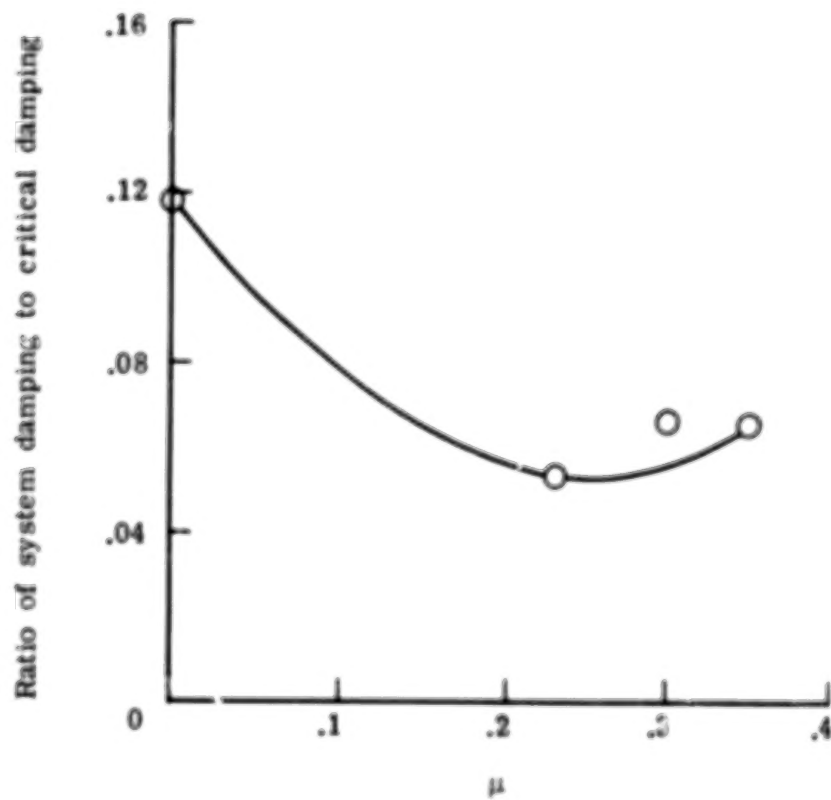


Figure 31.- Variation of lead-lag damping with advance ratio for stiff-pylon mounting. $\Omega = 64.4$ rad/s;
 $\delta_3 = 0^0$; $K\zeta = -0.1$; $C_L/\sigma = 0.06$.

90

50

END

5.19 78